POLITECNICO DI TORINO
Repository ISTITUZIONALE

Tutorial: A Versatile Bio-Inspired System for Processing and Transmission of Muscular Information

(Article begins on next page)

23 April 2024

Tutorial: A Versatile Bio-Inspired System for Processing and Transmission of Muscular Information

Fabio Rossi, *Graduate Student Member, IEEE*, Andrea Mongardi, *Member, IEEE*,
Paolo Motto Ros, *Member, IEEE*, Massimo Ruo Roch, *Member, IEEE*,
Maurizio Martina, *Senior Member, IEEE*, and Danilo Demarchi, *Senior Member, IEEE*

Abstract—Device wearability and operating time are trending topics in recent state-of-art works on surface ElectroMyoGraphic (sEMG) muscle monitoring. No optimal trade-off, able to concurrently address several problems of the acquisition system like robustness, miniaturization, versatility, and power efficiency, has yet been found. In this tutorial we present a solution to most of these issues, embedding in a single device both an sEMG acquisition channel, with our custom event-driven hardware feature extraction technique (named Average Threshold Crossing), and a digital part, which includes a microcontroller unit, for (optionally) sEMG sampling and processing, and a Bluetooth communication, for wireless data transmission.

The knowledge acquired by the research group brought to an accurate selection of each single component, resulting in a very efficient prototype, with a comfortable final size (57.8 mm x 25.2 mm x 22.1 mm) and a consistent signal-to-noise ratio of the acquired sEMG (higher than 15 dB). Furthermore, a precise design of the firmware has been performed, handling both signal acquisition and Bluetooth transmission concurrently, thanks to a FreeRTOS custom implementation. In particular, the system adapts to both sEMG and ATC transmission, with an application throughput up to $2 \, \mathrm{kB \, s^{-1}}$ and an average operating time of 80 h (for high resolution sEMG sampling), relaxable to $8 \, \mathrm{B \, s^{-1}}$ throughput and about 230 h operating time (considering a 110 mAh battery), in case of ATC acquisition only.

Here we share our experience over the years in designing wearable systems for the sEMG detection, specifying in detail how our event-driven approach could benefit the device development phases. Some previous basic knowledge about biosignal acquisition, electronic circuits and programming would certainly ease the repeatability of this tutorial.

Index Terms—Bio-inspired Electronics, Surface Electromyography, Bluetooth Low Energy, Event-based, Information Synthesis, Power Efficiency, Wearable System

I. INTRODUCTION

From its first clinical use in 1966 until now, the surface ElectroMyoGraphy (sEMG) technique still maintains its essential place in the list of medical procedures to investigate the health of the human body. Indeed, by placing bio-potential electrodes directly on skin surface, sEMG provides an accessible way to monitor the electrical activity of skeletal muscles [1], [2]. During the last 30 years, beyond the constant evolution of sEMG in clinical applications [3]–[5], its practice also branches, reaching different non-medical sectors [6], e.g., fitness monitoring [7], (therapeutic) gaming control [8], virtual reality interaction [9], human-machine interface [10], [11], speech [12] and gesture [13], [14] recognition.

Consequently to the sEMG applications spreading, related scientific publications [15], [16] describe the potentialities and diversities in developed sEMG systems: indeed, digging into the multitude of published documents, we can understand how the technology progress allowed the realization of functional and efficient solutions [17]–[20]. By analyzing current sEMG works [21], [22], focusing on State-of-Art (SoA) wearable systems, we tried to extract from all of them the common functional features, identifying the following ones as application-key aspects [14]:

- Accurate representation of muscular activity [23], [24]: good signal detection with respect to environmental noise sources (i.e., Signal-to-Noise Ratio (SNR) in 10 dB–30 dB range) and sufficiently representative digitization level (i.e., analog to digital conversion on 12 bit–24 bit);
- Fast system response to input variability: the overall application latency has to fulfill the real-time constraints (i.e., 100 ms to 300 ms) requested by the user application [25];

- Miniaturization of the final device dimensions: packaging all the system components in a small, light, and comfortable solution in order to monitor bio-signal activities without any bias due to the wearable device;
- Robust and accessible data streaming [7]: the wireless transfer of the data has to be stable over-time while providing a standard and versatile interface with smart devices (e.g., smartphone, smartwatch);
- Sufficiently long operating time: multi-days human activities monitoring could be investigated by using power-efficient devices able to work continuously without a frequent recharge of the battery.

However, although we can quickly summarize these milestones in a five-points list, to the best of our knowledge, many literature works [26]–[31] struggled to integrate all of them into a single optimized solution. Among the reasons, accurate signal digitization increases the amount of data to be processed and transmitted, thus impacting on device power consumption. Miniaturization (avoiding dedicated microchip) often brings to circuitry simplification, which relies on signal quality. Low-energy wireless transmission could be a bottleneck in terms of data payload, which could be overcome by wiring the connections, but sacrificing sensor wearability. Dedicated user applications [17]–[19], [21] can solve some of the above issues, but generally losing the possibility to be implemented in different configurations.

Therefore, looking at this complex scenario, this paper shares our experiences in facing these challenges: in particular, we tried to make all the listed features to converge into a single developed system, which, by taking the advantages of event-driven bio-inspired electronics [32], addresses the above problems towards feasible solutions. Our idea is to apply the Average Threshold Crossing (ATC) technique [33], which basically extracts threshold crossing events from the amplified and filtered sEMG signal, to monitor muscular activation with reduced processing and transmission data load, leveraging on power consumption and operating time.

Moreover, we designed our system focusing on its versatility. Considering that our research sEMG activities cover different fields, from SoA applications (e.g., low-power muscle and force monitoring [33], [34], hand gesture recognition [35]–[37], control of Functional Electrical Stimulation (FES) [38]–[41]) to emerging ones (e.g., muscle synergies analysis, facial sEMG), we developed a prototype taking into consideration multiple needs. For this reason, in parallel to the ATC extraction, we decided to maintain available to the user the sEMG information. Minimal hardware and firmware modifications could still be necessary for the proper functioning of each application, but the proposed system core could be maintained stable without any substantial variation.

Finally, we equipped our system with Bluetooth 4.2 wireless transmission to provide a standard interface with any devices, thus further fostering system applicability far from our studies.

Some practical operating setups are represented in Fig. 1: the proposed device can be applied as a stand-alone module for the discrimination of the activity of individual muscle (red boards), or it can be embedded in user-designed body networks for the recognition of hand-forearm gestures (gray
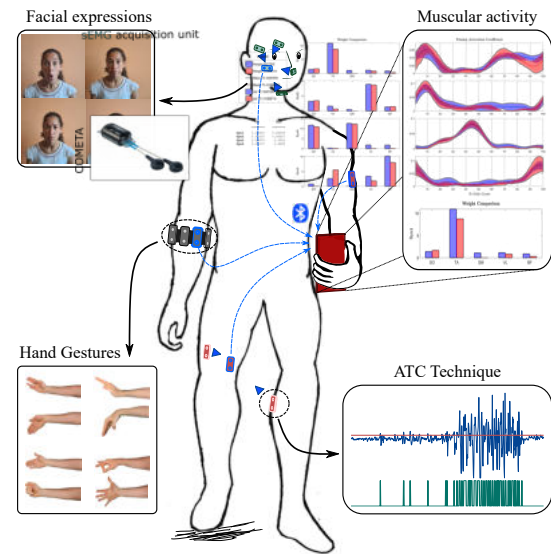

Fig. 1. Application scenarios: the wearable sEMG/ATC sensing node could be used as stand-alone module or combined in multi-board networks (wired or wireless) for hand gesture or facial expression recognition.

armband) or the decoding of speech and facial expressions (sea-green devices) by assessing the synergistic activation of near muscles domains.

The paper is structured as follows: Section II introduces the ATC technique, giving a brief review of significant outcomes and related advantages; Section III analyzes how the proper definition of each system component and implemented technology impacts the design and developing phases; Section IV and Section V go into details of proposed bio-inspired hardware, firmware and communication implementations; Section VI shows our results in terms of detected signal quality, parameters reliability and device power consumption; Section VII investigates how the proposed solution relates with similar devices; lastly, Section VIII concludes the paper.

II. AVERAGE THRESHOLD CROSSING: A JOURNEY INTO THE LAST DECADE OF OUR RESEARCH

The need for efficient solutions, able to overcome the current challenges in the design of bio-signal acquisition systems, led our investigations to define the event-driven Average Threshold Crossing (ATC) approach. Three design paradigms have been taken into consideration for the conception of this technique [32], combining them in order to complement the functionalities of each other in a unique solution:

- Bio-inspired: looking at the biological system, we aim to mimic the neural spikes communication by coding electronic signals in the form of digital pulses (i.e., the quantitative information is mapped onto the time domain as spikes series).
- Event-based: the *event* is identified as the informative phenomena related to a specific task; by building our system to act only as a consequence of events detection,
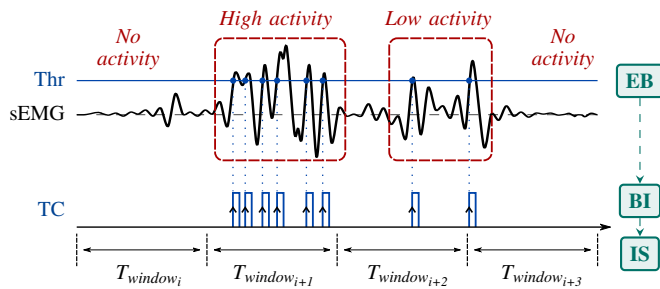
Fig. 2. Average Threshold Crossing (ATC) technique: following the Event-Based (EB) paradigm, the threshold crossing (TC) points are identified as the *events* carrying the information of muscle activation, and they can be represented with a time-distribution of electrical spikes, as it happens in the biological communication among neuron cells, i.e., a Bio-Inspired (BI) process. Information Synthesis (IS) is achieved by applying a time-window (T_{window}) approach on the TC distribution in order to compute the ATC parameter, which summarized the state of muscle contraction (e.g., high, low or no activity).

we aim to limit the power consumption to event-coded actions.

- Information synthesis: the overall amount of acquired data could be drastically reduced by achieving a feature extraction process directly on the sensor node (i.e., edge-computing), thus lowering transmission payload while providing high-level user information.

Fig. 2 clearly depicts the definition, implementation, and advantages of the ATC technique, pointing out where the above paradigms take action: our idea is basically to compare the sEMG signal, once it has been amplified and filtered, with a threshold; we define as *informative event* every time the signal overcomes the threshold (i.e., event-based). From the events distribution (i.e., bio-inspired), we compress the Threshold Crossing (TC) information (i.e., Information synthesis) by counting how many events have been generated in an observation window (later also referred as ATC window), consequently defining the ATC parameter as in Eq. 1, where $\#TC_{events}$ states for the number of TC events and T_{window} normalizes the parameter to the duration of the observation window.

$$ATC = \frac{\#TC_{events}}{T_{window}} \qquad (1)$$

As also reported in [42], [43], ATC and other similar techniques, e.g., Zero-Crossing (ZC), Wilson Amplitude (WAMP), fit particularly well to the sEMG signal because of their amplitude proportionality and incremental variability in presence of muscle activity (i.e., bio-inspired). Thus, the ATC parameter could be designed as a useful indicator for monitoring the muscle behavior.

In our first work [44], we investigated the feasibility of using the ATC parameter in monitoring the force exerted by muscles: both the ATC parameter and the Absolute Rectified Value (ARV), identified as gold standard sEMG estimator for force evaluation, have been examined. Experiments were conducted on eight subjects pushing a dynamometer up to 70 % of their Maximum Voluntary Contraction (MVC); ARV and ATC trends have been extracted (observation window of

500 ms) from sEMG signals acquired by forearm muscles; the overall average correlation has been computed for both the ATC-force and the ARV-force pairs obtaining values of 0.95±0.02 and 0.97±0.02 for respective comparisons. Continuing in the same direction, in [45] we demonstrated how the measured correlation maintains an acceptable value above 0.9, although the 70 % of the TC events are lost. Therefore, although the ATC-force correlation decreases for low MVC values (< 23 %), the ATC-force and ARV-force comparisons do not show significant differences, also presenting a solid robustness to event losses, so opening the road to the use of ATC as a reliable force estimator.

In two consecutive works [33], [46], we went deeper in the study of the ATC-force relation trying to discriminate different force levels performing standardized isometric contractions with a set of weights. Results on ATC extraction (ATC window of 130 ms) confirmed the possibility to discern among three coarse levels: natural load (0 kg), low activation state (2 kg, 4 kg and 6 kg), and high activation state (8 kg and 10 kg). From these tests, we also found that the optimization of the threshold per subject (six in total) has an effect on lowering the overlap among ATC values related to different weights.

As it seems clear, the choice of the right threshold value is relevant on the extraction of TC events. Indeed, a proper threshold has to detect as many sEMG events as possible so to get all the information content while maintaining strong robustness to the environmental noise and bio-signal related artifacts. As we will demonstrate in Section V-A, after different investigations [40], [47], we found that setting the threshold just above sEMG signal baseline, during muscle rest condition, permits us to detect the most relevant muscle activation events with minimal effort.

The possibility to determine different force levels based on the ATC parameter led our research activities to evolve toward the study and development of human-machine interfaces based on ATC. In [35] and [37] we investigated the performance of some machine learning algorithms for the recognition of hand gestures: a specific configuration of the acquisition electrodes allowed us to classify six gestures by employing only three ATC channels, proving the effectiveness of the event-based approach in supporting, as a feature extraction stage, AI-based applications. In the same studies, we also tested the advantages of an embedded implementation of such algorithms in order to move the entire ATC feature extraction and gesture classification directly on a wearable system.

After demonstrating the usability of ATC, next step was to focus on the design of an sEMG-ATC acquisition system. In [34], [46] we analyzed how the definition of the device architecture, which follows the standard functional blocks of analog acquisition channel, digital interface, and wireless connectivity, could be reviewed by implementing the ATC.

Starting from the feature extraction, we were able to perform this process directly on the acquisition channels, since the generation of the TC signal can be achieved simply using a voltage comparator on the amplified sEMG signal. Moreover, due to the *quasi-digital* properties of the TC signal (i.e., digital signal shape, time-analog information), the events count (i.e.,
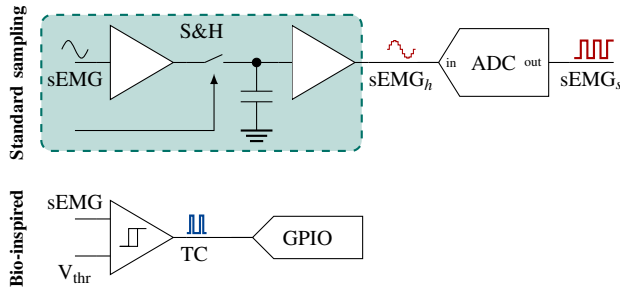
Fig. 3. Differences between the standard sampling approach and the combination of the event-based and bio-inspired methodologies: in the first case, the Sample and Hold (S&H) block is generally required to hold the muscle signal (sEMG$_h$) previous its Analog-to-Digital Converter (ADC) digitization (sEMG$_s$); in contrast, our proposed circuit compares the analog sEMG signal with a voltage threshold to generate the TC signal, which is subsequently driven at the GPIO input for the ATC computation.

ATC) could be computed by directly connecting the TC signal to standard input/output (I/O) interfaces of a microcontroller, thus not requiring any Sample and Hold (S&H) and Analog-to-Digital Converter (ADC) additional interfacing circuitry. Therefore, as depicted in Fig. 3, by applying the event-based and bio-inspired paradigms, we were able to move the feature extraction process from the firmware (FW) or software (SW) domain, as usually done, to the HW one: this modification distances the ATC technique from the similar ZC and WAMP parameters, which usually require to sample sEMG data and to process them only after digitization [43]. In this way, minimizing the HW and SW/FW resources required to extract the sEMG feature, we limited the related power consumption and the computational effort. These modifications have been implemented both realizing an Application Specific Integrated Circuit (ASIC) [33] and developing a Printed Circuit Board (PCB) with Commercial Off-The-Shelf (COTS) components [46] in order to demonstrate the HW versatility of this approach.

Focusing now on the wireless domain, in [35] we demonstrated how, employing the widespread Bluetooth Low Energy (BLE) short-range communication protocol (standard 4.0 [48]), we were able to save up to 14 % of a defined power budget (i.e., ~20 mW) transmitting the information of four ATC channels w.r.t. just one of sampled sEMG. Essentially, this behavior is strictly related to the application throughput of above methodologies, as graphically represented in Fig. 4: as required by the Nyquist-Shannon theorem, the sEMG signal has been sampled at 1 kHz (considering its frequency spectrum [24]) with 12 bit ADC resolution, thus obtaining a data transfer rate of 2 kB s^{-1}; in contrast, the ATC approach, taking advantages of its intrinsic information synthesis, brings to a significant reduction of the recording data, which, considering an ATC window of 130 ms, results in a throughput of 28 B s^{-1}. However, although the benefits of an event-driven approach are clearly visible in terms of transmitted data (about two order of magnitude less), we discovered that, even optimally setting the BLE connection parameters for individual cases (sEMG and ATC), the BLE wireless standard could limit the real applicability of our design paradigms (i.e., event-based,
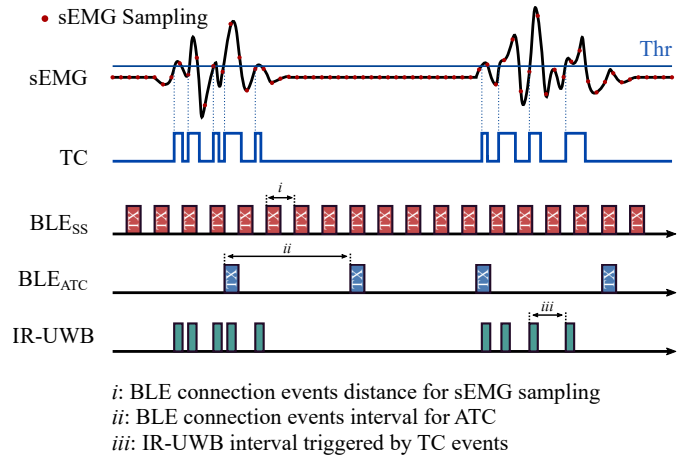

i: BLE connection events distance for sEMG sampling
ii: BLE connection events interval for ATC
iii: IR-UWB interval triggered by TC events

Fig. 4. Wireless transmission for sEMG and ATC: considering the BLE protocol, the common sampling (BLE$_{SS}$) approach needs a dense distribution of connection events in order to successfully transmit (TX) sEMG data; on the other hand, the window approach of the ATC technique (BLE$_{ATC}$) relaxes the timing of the transmission. Moving away from standard protocols, IR-UWB perfectly fits an event-driven transmission since each TX occurrence is directly triggered by threshold crossings.

bio-inspired, information synthesis). Indeed, the possibility of directly transmitting the TC events in real-time, only in the presence of muscle activity (i.e., event-based transmission), can not be consistently achieved considering the connection timing management implemented by the BLE stack, which sets 7.5 ms as the minimum distance among connection events [49]. On the other side, although the overhead structure of a BLE packet (i.e., 21 B [50], [51]) mismatches with the minimal data rate supported by the ATC technique, the transmission of the ATC parameter is not affected by the protocol timing constraints because of the relaxed window approach, which in the worst case could cause a slight jitter of one connection event in the ATC reconstruction.

A more efficient but less commonly employed (and not standard) solution could be represented by the Impulse-Radio Ultra-Wide Band (IR-UWB) technology [33], [44], [45], [47]: as shown in the lower axes of Fig. 4, IR-UWB pulses can be directly triggered by TC events, allowing the TX to send data only in presence of muscle activation. In this way, the limitation of a real-time TC transmission could be overcame, but with the downside inherent to the loss in interoperability because of a full-custom transceiver and protocol. In [45] we presented how to extend this configuration to a multi-channel system using dedicated address event representation, which can be easily involved lab-on-chip bio-sensing measurements [52].

III. SYSTEM LEVEL ARCHITECTURE

The definition of the most suitable framework for the development and implementation of the proposed sEMG ATC-based system needs to cover four main aspects:

1) Circuits and systems for sEMG detection;
2) Feature extraction technique;
3) Digital interface;
4) Wireless connectivity.

TABLE I
MCUs COMPARISON FOR DIGITAL SELECTION

	Apollo3 Blue [53]	nRF52840 [54]	CC2642R [55]	STM32WB55 [56]	QN9080-001 [57]
Clock frequency	48 MHz	64 MHz	48 MHz	64 MHz	32 MHz
Power efficiency (typ.)	$6\,\mu A\,MHz^{-1}$	$52\,\mu A\,MHz^{-1}$	$71\,\mu A\,MHz^{-1}$	$53\,\mu A\,MHz^{-1}$	$34\,\mu A\,MHz^{-1}$
Flash/ROM	1024 kB	1024 kB	352 kB	1024 kB	512 kB
RAM	384 kB	256 kB	80 kB	256 kB	128 kB
TX current (typ.)	3 mA @ 0 dBm	4.8 mA @ 0 dBm	7.3 mA @ 0 dBm	5.2 mA @ 0 dBm	3.5 mA @ 0 dBm
Package	4.5 mm x 4.5 mm	7 mm x 7 mm	7 mm x 7 mm	7 mm x 7 mm	6 mm x 6 mm

All devices feature an Arm® 32-bit Cortex®-M4F CPU, Bluetooth 4.2 standard, and 1.8 V power supply.

Considering the scenario described in section II and defining the ATC parameter as our muscle monitoring feature, we aim for the co-design of points 1) and 2) into a single solution due to their strict symbiotic dependence. Since the TC signal is extracted by comparing the amplified and filtered sEMG signal with a threshold, we have to evaluate the proper HW bio-signal conditioning circuits (e.g., amplifiers, filters) for the processing of the raw signal. Besides, keeping in mind the advantages of the event-driven approach and the possibility to extract the TC signal in HW (lowering FW computational effort), we decided to add also the electronics for the TC generation at the end of the sEMG-conditioning chain. On the other hand, filters and amplifiers design rules and best practices (e.g., filter order, bandwidth ripple, bandwidth-gain product) can be appreciably relaxed considering the implementation of the subsequent thresholding process, thus allowing us to reduce the complexity of the entire circuit.

Point 3) could be investigated considering application functionalities (e.g., data acquisition, processing and transmission) and system configurable settings (I/O communication with microchips, antenna, etc.) while focusing on low-power and energy efficiency aspects of the final solution. Therefore, we opted for using a MicroController Unit (MCU) as an adequate choice to join together all these tasks.

The above considerations bring directly to the definition of point 4) since the selected MCU has to support the suitable wireless standard. Among the expansive list of available commercial protocols (e.g., Bluetooth, Zig-Bee, Wi-Fi, IEEE 802.15.4, Thread), we looked at Bluetooth (low energy version 4.2 [49]) because of its low power features, flexible through-put, widespread adoption, and also considering the discussed feasibility of the ATC-BLE transmission [35]. Table I reports the fundamental features of commercial MCUs, filtered out from the vast sea of available devices searching for the ones able to satisfy above requirements. In particular, all selected MCUs have a Central Processing Unit (CPU) based on an ARM® 32-bit Cortex®-M4 with Floating Point Unit (FPU), support Bluetooth 4.2 wireless protocol or newer, feature similar peripherals (e.g., ADC, Serial Peripheral Interface (SPI), Universal Asynchronous Receiver Transmitter (UART), timer), and their power supply can be lowered to 1.8 V for low-power applications. Among comparison features, the main clock frequency and the related power efficiency are the most significant because they represent how fast the CPU

processes the operations at fixed current absorption per MHz. Wireless transmitter (TX) output level strongly affects power consumption during continuous data streaming, thus looking for the best power efficiency could improve battery lifetime. MCU physical size had been taken into consideration too, since the component package could impact on final device area.

Furthermore, non volatile (e.g., Flash) and volatile (e.g., RAM) memories need to be sufficiently large to store application data and to enable the proper firmware performance in edge-computing tasks. Indeed, since the proposed system can be employed in several different applications (as already highlighted in Section I, Fig. 1), although the ATC itself implies a very low computational overhead, the MCU has to be chosen powerful enough to handle relatively high amount of data with fast response time. For example, considering the on-board computing performed during gesture recognition [37], the RAM memory has to be large enough to contain all the parameters needed by the neural network to predict the movements, while ensuring a fast response to allow the CPU to handle the predictions in real time.

Therefore, analyzing above specifications all together, we identified the AmbiqMicro Apollo3 Blue [53] as the MCU which fulfills our requirements with the best trade-off among discussed features. Looking at its characteristic, it requires low current absorption of $6\,\mu A\,MHz^{-1}$ for the CPU (running up to 48 MHz) and 3 mA TX power transmitting at 0 dBm, it has a RAM availability of 384 kB and fits into $20.25\,mm^2$.

In conclusion, our system level architecture has been defined as follows: a custom sEMG-ATC analog conditioning circuit for acquisition and feature extraction, the Apollo3 Blue as MCU for digital control of the system and the Bluetooth 4.2 as wireless standard for data transmission. As design rules, focusing on extending device operating-time as much as possible, we accurately select each component looking at its power consumption, and we fixed power-supply (V_{DD}) to 1.8 V.

IV. FRONT-END FOR sEMG PROCESSING

As clarified in section III, by realizing our custom sEMG conditioning circuit we are able to extract the event-based signal information (i.e., threshold crossings) directly in hardware. Fig. 5 shows the latest version of our sEMG front-end, which has been obtained as result of our strengthened knowl-
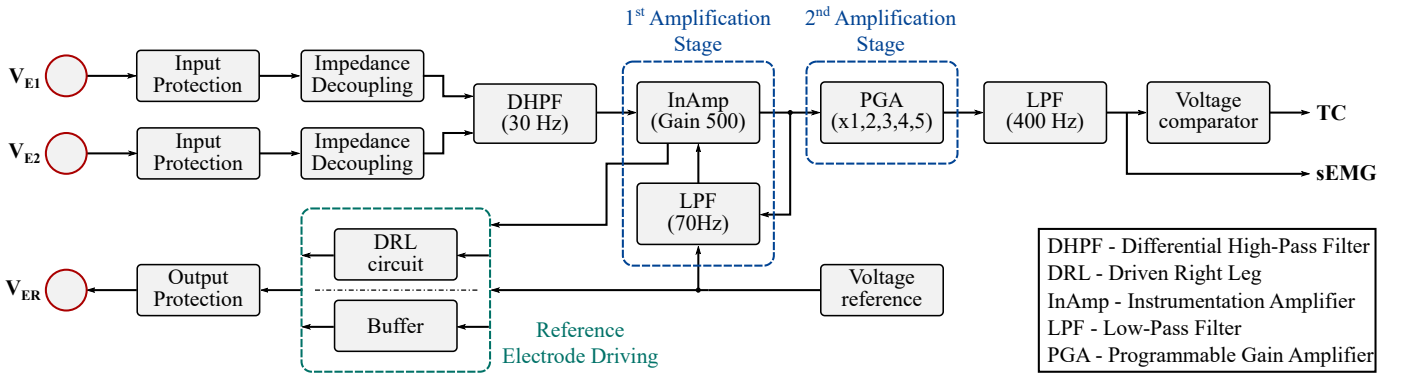
Fig. 5. Schematic block diagram of the proposed Analog Front End (AFE): the complete chain provides a variable amplification ($\times 500 - \times 2500$) of the sEMG signal in the 30 Hz to 400 Hz range, and performs the extraction of the TC signal as last stage.

edge in bio-electronic acquisition field over years. The front-end works with the typical bipolar electrodes configuration [2], i.e., using two sensing electrodes to sense myofibers depolarization (V_{E1}[1] and V_{E2}) and one to refer body potential w.r.t. acquisition device (V_{ER}) [58]. All blocks have been designed using commercial off-the-shelf components to demonstrate the complete feasibility of our approach (no custom microchip) and, considering the absence of digital circuitry (with the exception related to how TC threshold has been handled), we can define the proposed acquisition channel as an Analog Front-End (AFE).

Next (sub-)sections focus on each AFE block, both explaining its functionality and describing which design rules we followed during front-end realization.

A. Input/Output Protection

Excessive voltages, especially if much higher than supply voltage (V_{DD}, i.e., 1.8 V), could damage on-board circuitry components, whose absolute maximum ratings are normally close to V_{DD}. Therefore, good practice imposes the insertion of a protection circuit able to limit the effect of undesired voltages. Our proposal is represented in Fig. 6.

As first AFE protection stage we designed an R-D network: R_1 and R_2 account for high-voltage drop in order to have safer

---

[1] All node potentials are considered with respect to the common reference of the circuit, i.e., the negative terminal of the battery.

$R_1 = R_2 = 10\,k\Omega$, $R_3 = R_4 = 2.2\,k\Omega$
$R_5 = 330\,\Omega$, $L_1 = L_2 = $ BLM15AX102SN1D
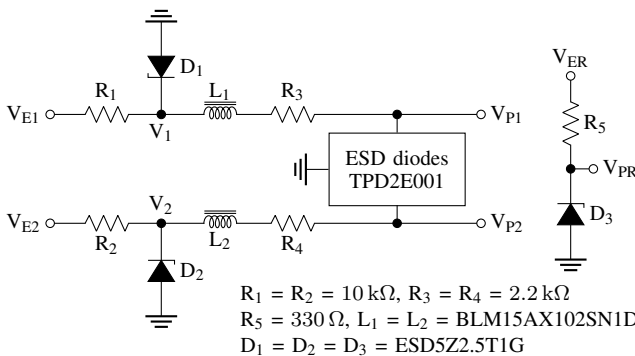$D_1 = D_2 = D_3 = $ ESD5Z2.5T1G

Fig. 6. Input/output protection: the damage of the circuitry caused by overvoltage inputs is limited using R-D networks; the high-frequency environmental noise is attenuated by using ferrite beads.

V_i voltages while D_1 and D_2 provide preferential ground paths when V_i overcome diodes breakdown voltages, thus avoiding higher voltages in downstream circuitry.

Ferrite beads L_1 and L_2 suppress high-frequency electromagnetic and electrical interferences. R_3 and R_4 resistors limit inward currents in the Electro-Static Discharge (ESD) protection module, which completes our input protection block.

From a design point of view, in order to maintain limited voltages at v_1 and v_2 nodes, R_1 and R_2 resistors have to observe the relation in Eq. 2, where V_{in} is the AFE input (over)voltage, V_{br} the Zener diode breakdown voltage and I_{max} the maximal current acceptable by ESD module.

$$R = \frac{V_{in} - V_{br}}{I_{max}} \qquad (2)$$

In critical scenarios, V_{in} can reach tens to hundreds of V (e.g., when AFE is coupled to a FES stimulator [41]), thus reducing V_{in} - V_{br} to V_{in}. In these situations, resistors value has to be chosen adequately w.r.t. I_{max} limitation and, considering the relative high $V_{in} \cdot I_{max}$ product in case sustained overvoltages occur, featuring $1/4$ W power dissipation.

A similar protection has been also designed for the reference electrode, here mainly focusing on current limitation (through R_5 resistor), which has been maintained below 10 mA in order to avoid physical damages or annoying perceptions to the user.

B. Decoupling Circuit

Two voltage followers, one for each sensing channels (see Fig. 7), have been inserted between input protections and signal conditioning. Main tasks at this stage are both to provide the proper impedance to the amplifier inputs, decoupling them from electrode-skin impedance, and to guarantee sEMG integrity.

C. Differential High-Pass Filter

The electrode-skin interface represents a very delicate area where ionic flows are transformed into electrical currents by means of redox reactions at electrode metal surface. As
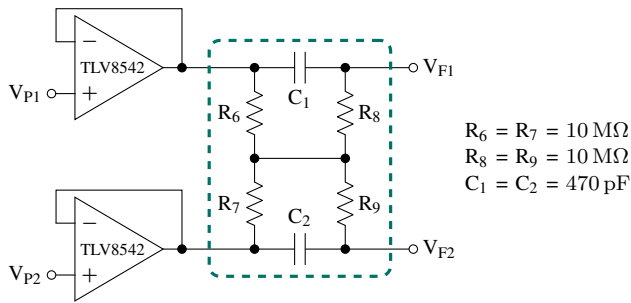
Fig. 7. The designed differential high-pass filter limits the effect of the movement artifacts avoiding the saturation of the on-board electronic components.
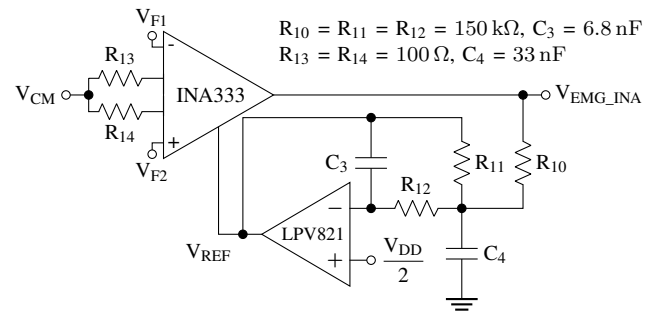

Fig. 8. First amplification stage: Instrumentation Amplifier (InAmp) carries out the difference between inputs, obtaining the differential signal of interest, which is further stabilized by low-pass negative feedback on the reference voltage.

follows, any chemical or physical disturbances can drastically affect the quality of acquired signal, also considering its extremely reduced amplitude at source location. Among them, movement artifacts, usually induced by cables motion (in standard application electrodes are wired connected to amplification stage), has been demonstrated to introduce low-frequency noise below 20 Hz-30 Hz [59], [60]. Also improving interface stability, e.g., electrolyte gel facilitating carriers flow, glue for stable electrode attachment, does not overcome such phenomena. Therefore, possible solution concerns to attenuate these artifacts by filtering out noise frequencies at AFE inputs.

We inserted a first order Differential High-Pass Filter (DHPF), designed following indications reported in [61], before the instrumentation amplifier (see Fig. 7), so avoiding movement artifacts amplification and the saturation of consecutive electronic components. Appropriate resistors and capacitors values have been calculated solving Eq. 3, where cutoff frequency f_c has been set to 30 Hz since we found this value to be an optimal trade-off between artifact removal and sEMG energy-frequency integrity.

$$f_c = \frac{1}{2\pi R_8 C_1} = \frac{1}{2\pi R_9 C_2} \tag{3}$$

In our experience, we also tried to raise f_c to 60 Hz or 70 Hz in order to attenuate power-line interference (i.e., at 50 Hz or 60 Hz, based on the country) at this stage. However, due to the low order of the filter and the possible components mismatch, this configuration demonstrated its effectiveness in reducing the 50 Hz and 60 Hz contributions but attenuating to much the sEMG energy content and resulting in very poor signal quality. For this reason, the cutoff frequency of the DHPF has been maintained to 30 Hz.

D. Instrumentation Amplifier (1st Amplification Stage)

Bio-signal amplification is needed in order to be able to process the signal using digital electronics. For sEMG, required gains varies depending on recording muscle conditions (e.g., superficial or deep fibers, covering fat layer, fibers orientation, muscle mass and body volume) covering a 500 V/V to 6 kV/V value range [60]. Moreover, total amplification is usually divided into two or more stages: in this way, from one side, AFE is adequately set to record electrical activity from different muscle types; from other side, gain division relaxes amplifier gain-bandwidth constraints,

avoiding signal distortions.

In our solution, we designed a first amplification stage, reported in Fig. 8, using an Instrumentation Amplifier (InAmp), suitable to carry out the differential (bipolar) acquisition of sEMG signal. Basically, InAmp performs the subtraction between input channels, and amplifies this difference by the differential gain A_d, i.e., $V_{EMG\_INA} = A_d(V_{F2} - V_{F1}) + V_{REF}$, centering it to the middle of the voltage supply (V_{REF}). As general features, InAmp provides high Common Mode Rejection Ratio (CMRR) in order to reject as much as possible common noises sources (e.g., power-line interference) while detecting inter-electrode variation (i.e., sEMG signal).

Depending on the internal architecture of the InAmp, A_d gain could be easily set through an external resistor (usually named R_g). In our AFE, we followed this road, i.e., using the INA333 from Texas Instruments, physically splitting the R_g value into the two R_{13} and R_{14} resistors, thus also enabling the driving of the sEMG common-mode (V_{CM}) to the DRL circuit. We defined $A_d = 500$ V/V as default amplification value since it allows us to achieve good signal acquisition (when superficial or large muscles are considered) while maintaining constant amplification in the 0 Hz to 400 Hz range [62].

Looking at real-case scenarios, electrical and environmental noise sources (here intended as common-mode) are not completely rejected by InAmp because both real amplifier behavior has limited performances, and common-mode can be transformed into differential signal (and so amplified by A_d) by electrodes path and circuit unbalances [63]. In such circumstances, amplified sEMG could be corrupted by overlapping noise, making its interpretation difficult and misleading.

Furthermore, in order to make the output of the InAmp more stable and consistent, we added a negative feedback on the InAmp reference: it consists of a second order Butterworth multiple-feedback low pass filter with cutoff frequency f_c [64], as calculated in Eq. 4.

$$f_c = \frac{1}{2\pi\sqrt{R_{11}R_{12}C_3C_4}} \tag{4}$$

Generally, the idea is to sense the InAmp output, filter unwanted noises and, after its inversion, feed it again to the
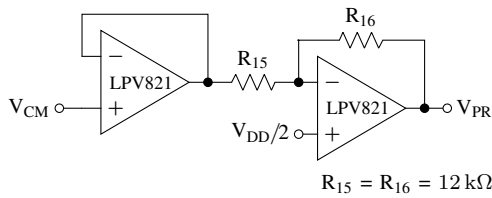
Fig. 9. The Driven Right Leg (DRL) circuit has been designed as a cascade of a common mode stabilization buffer and an inverting amplifier.

InAmp reference. In this way, output signal baseline follows noise variations but, being 180 degree out-of-phase, is able to remove such interference. In our first prototype, f_c was set to 10 Hz in order to account only for the low-frequency noise introduced by the InAmp itself. In newest versions, we have risen f_c to 70 Hz to take into account also the power-line interference (as previously tested at the DHPF stage without improvements) which, depending on the environmental conditions, is not completely rejected by the InAmp itself. Contrary to our tests about DHPF response, the negative feedback on the InAmp reference works as expected in the attenuation of disturbances below 70 Hz without significantly affecting the energy of the detected sEMG signal.

E. Reference Electrode Driving

As it can been seen from diagram on Fig. 5, voltage for reference electrode can be driven using two testing circuits.

The first (and low complexity) solution provides a voltage reference by means of a voltage regulator. This value is fixed to $V_{DD}/2$ in order to provide a body reference voltage (V_{ER}) matching the one driven to InAmp. Its value is further stabilized by the insertion of a voltage follower before electrode interface.

The second possibility consists in the well-know Driven Right Leg (DRL) circuit [60], [63], [65], which limits the effect of common-mode noise when it is relevant on subject body.

Among high variety of DRL designs [66]–[70], we focused on low complexity, proposing the solution represented in Fig. 9: first of all, we drive the V_{CM} to a voltage follower; then we feed an inverting amplifier with unitary gain ($R_{15}=R_{16}$) in order to obtain a reversed common-mode voltage, referred to the middle of power supply, to be injected back to subject body through the reference electrode (E_R).

Both the solutions end with the safety circuit introduced in section IV-A (Fig. 6), which limits the maximal current flowing through E_R at 10 mA.

F. Programmable Gain Amplifier (2nd Amplification stage)

A second amplification stage is often required when default gain is not sufficient to adequately represent muscle activity of deeper or smaller myofibers [60]. Hence, we designed a Programmable Gain Amplifier (PGA), reported in Fig. 10, which provides ×2, ×3, ×4 and ×5 additional amplification values.

$R_{17} = 487\,k\Omega$, $C_5 = 12\,nF$ $R_{18} = 243\,k\Omega$, $C_6 = 22\,nF$
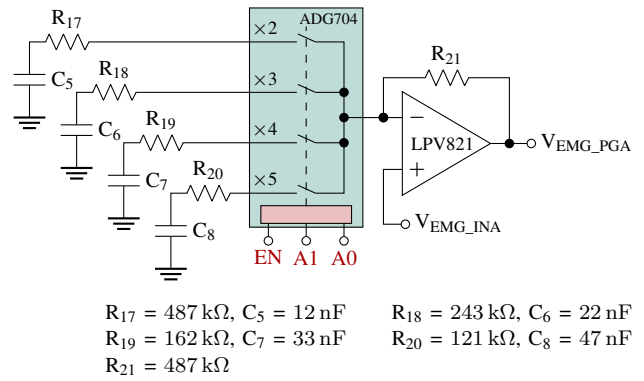$R_{19} = 162\,k\Omega$, $C_7 = 33\,nF$ $R_{20} = 121\,k\Omega$, $C_8 = 47\,nF$
$R_{21} = 487\,k\Omega$

Fig. 10. Programmable Gain Amplifier (PGA): adaptable amplifier gains (i.e., ×2, ×3, ×4 and ×5) are obtained by controlling the analog multiplexer on the amplifier inverting branch.

With the goal to maintain AFE at low complexity, while giving to the user an easy control of acquisition parameters, we realized this stage using an analog multiplexer which, depending on its digital inputs (A0, A1), provides a different electrical path (corresponding to the desired gain value) to the negative input of the operational amplifier. Each path consists in an RC circuit, acting as an high-pass filter ($f_c \simeq 30$ Hz) in order to avoid the amplification of the signal baseline. When no additional gain has been requested (EN disabled), this stage works as a buffer for the sEMG signal. This custom configuration has been preferred to a COTS PGAs due to their higher power consumption and to the usual complexity of their internal design (i.e., commercial PGAs usually allow a wider range of gain values w.r.t. to the ones needed by our application).

G. Low-Pass Filter

A Sallen-Key Low-Pass Filter (LPF), represented in Fig. 11, is placed after amplification stages in order to limit sEMG signal bandwidth to 400 Hz, considering the most relevant energy content at 50 Hz–150 Hz [23].

The cutoff frequency f_c of this Butterworth Filter has been calculated in Eq. 5, according to [64].

$$f_c = \frac{1}{2\pi\sqrt{R_{22}R_{23}C_9C_{10}}} \tag{5}$$

This stage prevents the TC signal to be influenced by higher frequencies w.r.t. the ones related to muscle activity, and it matches the bandwidth amplification designed for previous

$R_{22} = R_{23} = 27\,k\Omega$
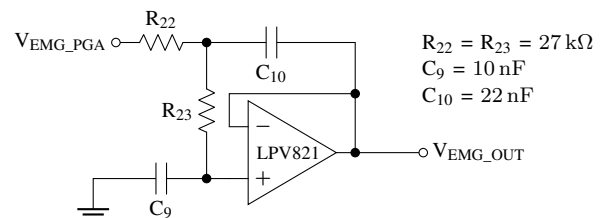$C_9 = 10\,nF$
$C_{10} = 22\,nF$

Fig. 11. The Sallen-Key Low-Pass Filter configuration centered at 400 Hz limits the sEMG bandwidth, acting also as anti-aliasing filter for the (optional) signal digitization.
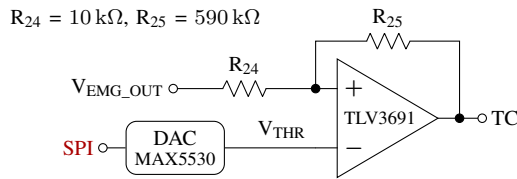
Fig. 12. Voltage comparator for the TC extraction with fixed hysteresis (30 mV) around V_{THR} value.

parts. Since the sEMG is also placed in input to an ADC at this stage, this LPF works also as an anti-aliasing filter (minimum sampling frequency of 800 Hz) [24].

H. Voltage Comparator

Finally, last stage of our AFE consists in a voltage comparator for the extraction of TC signal, as reported in Fig. 12. Since a different threshold value can be required depending on muscle activity and environmental conditions, we included a Digital-to-Analog Converter (DAC) for threshold generation. In this way, beyond the proper threshold setting, the digital control of DAC permits the user also to implement additional software routines for acquisition management.

A 30 mV hysteresis, centered around threshold value, transform the comparator into a more efficient Schmitt Trigger, solving the $V_{HYST} = V_{DD} \cdot R_{24}/R_{25}$ relation. Hysteresis helps us to prevent spurious spikes when signal is oscillating around threshold value, thus driving in the most clean way possible the digital path to the microcontroller dedicated input.

V. DIGITAL PART FOR SIGNAL PROCESSING

While the discussed AFE is the key component of the analog acquisition part, the digital part is the core of the processing section. The main actor is the Apollo3 Blue MCU, which, featuring an ARM Cortex®-M4F processor, can be involved both in wireless communication and artificial intelligence applications, efficiently reducing power consumption of the overall system.

In addition to the microcontroller, other components have been included in the system:

- A UART-to-USB converter, which allows the user to communicate with the microcontroller directly from a computer, enabling an easy interface for debug and firmware bootloading.
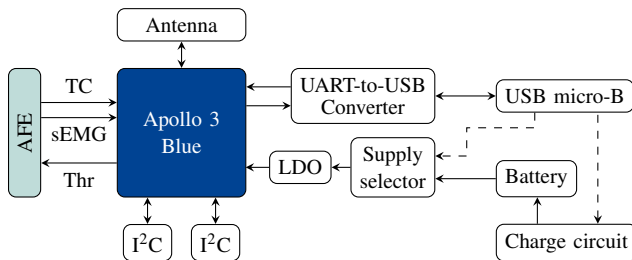

Fig. 13. Schematic block of the digital part: Apollo3 Blue represents the central core of the system, which processes the signals from the AFE, manages wireless communication through the BLE antenna and provides a standard interface with both USB (micro-B) or I²C connectors.

- Two I²C connectors (input/output), to make the board connectable in a chain bus;
- A DAC, which allows us to perform an accurate threshold calibration;
- A USB-powered battery charger, to complete the wearable scenario.

A schematic diagram of the connections among above peripherals with the MCU is reported in Fig. 13.

Regarding the firmware needed by the applications discussed here, the tasks that the microcontroller should be able to manage are divided in two main categories: generic peripheral handling for ATC evaluation, and user interface protocols. The first is functionally the same for each version of the system, being in charge of the configuration of peripheral parameters useful for ATC computation. The latter, instead, is more dependent on the target application and on the hardware configuration to be involved. In fact, according to required latencies and wearability, the design can vary from a serial, reliable and fast, connection (e.g., UART/RS232, I²C), to a more complete, but complex, wireless implementation (e.g., BLE, IR-UWB). Furthermore, if the application included artificial intelligence, proper routines would be integrated in the firmware to handle, e.g., recognitions and predictions.

Our present solution has been implemented thanks to the FreeRTOS real time operating system [71], able to virtually manage in a concurrent way both the ATC evaluation and the Bluetooth 4.2 communication to the central user device (e.g., a computer plotting data, a smartphone/smartwatch displaying muscles activation, an actuator performing movements based on a recognized gesture [36]), but other solutions could be equally effective, depending on the hardware used.

A. Peripheral handling for ATC evaluation

The microcontroller code is first configured for low power operations, exploiting proprietary libraries capabilities. The main clock frequency is reduced from the default 48 MHz to 24 MHz to further optimize power efficiency. The application does not require high frequency clock, thus if the microcontroller could go slower, a lower setting could have been selected.

Once the initial parameters are selected, the peripherals needed for ATC management are configured, including GPIO settings and on-board wired communications. First, the pin selected to receive the TC signal is configured as input, with interrupt on rising edge enabled. Then, a proper timer configuration has to be performed, setting it to make cycles of the desired duration (e.g., a common value is 130 ms [46]); since no excessive precision is needed to control the length of the window, a low frequency clock source can be selected, further relaxing the peripheral effort.

With the input port enabled, to complete the basic configuration, two more settings are required: the enabling of the serial ports needed by the SPI to control the DAC (Section IV-H), and the choice of the desired gain of the AFE, by configuring the PGA stage detailed in Section IV-F.

Then, threshold calibration has to be performed, in order to find the proper voltage value accordingly to environment and

subject condition. In fact, in ideal conditions, the threshold would be set 16 mV above the expected signal baseline, having to take into account only the lower half of the hysteresis, thus detecting every, even minimal, activation of the muscle. Unfortunately, real cases are affected by a lot of noise sources, making the baseline of the signal not always at the desired value (i.e., middle voltage supply) and with a possible uncertainty due to unfiltered noise. According to this, the threshold calibration, performed every time the system is switched on, is able to mimic the theoretical approach to the effective signal, finding the right delta above the signal noise to detect actual muscle activation and neglect spurious noise spikes.

The actual firmware routine, detailed in the flowchart of Fig. 14, is a finite state machine, which checks the detection of TC events and modifies the threshold value accordingly, by sending proper commands to the on-board DAC. In particular, depending on the state, the behavior is the following:

1) The threshold is decreased by 150 mV every second, while no event is detected. When an event arises, the state increases, leaving the threshold unmodified.
2) A further event is expected, to confirm the previous detection. If it is captured, the threshold is set higher than last value (i.e., +200 mV) and the next state would be state 3; if not, the flow is taken back to state 1, as previous detection was generated by a temporary noise source.
3) The fine tuning of the threshold begins, with a similar behavior w.r.t. state 1, but lowering the value by 10 mV steps.
4) Like in state 2, further events are expected, to confirm a proper identification of the signal baseline. The threshold is untouched in either case, and only the state changes, being set to 3 in case of a negative outcome and to 5 if it is positive.
5) last state still checks the effective detection of the baseline. The state is brought back to 3 if no event is captured, but if the detection is confirmed the threshold is raised of 40 mV (i.e., last decreasing step plus the comparator hysteresis) and the routine is terminated.

With the threshold value set, the initial configuration can be considered concluded. The actual ATC evaluation will then be triggered by the user, starting the timer and enabling the interrupt. The TC events will be counted and saved at the end of each time window, in the simplest way possible, as detailed in Fig. 15, thus avoiding ADC conversion and relaxing microcontroller hardware resources.

```
while TC acquisition is requested do
    count ← 0
    while waiting for an ATC window to end do
        if an interrupt arises then
            count ← count + 1
        end if
    end while
    TC_value ← count
end while
```

Fig. 15. TC count evaluation. Every time an event occur, the dedicated interrupt service routine is called and the event count is incremented. When the time window reaches its configured duration, the corresponding TC value is saved and the count is reset to 0.

B. User interface protocols

The remaining firmware routines are dedicated to user interface and debugging.

In a first prototyping phase, an UART connection (available through the on-board USB-to-serial converter) could be useful to send messages to a computer graphical user interface, thus displaying both data and critical information (e.g., peripherals malfunctions, BLE disconnection) and considerably speeding up device test and development. On the other hand, the final product would need a wireless communication system, in order to be quickly accessible regardless of the use case and without compromising the wearability.
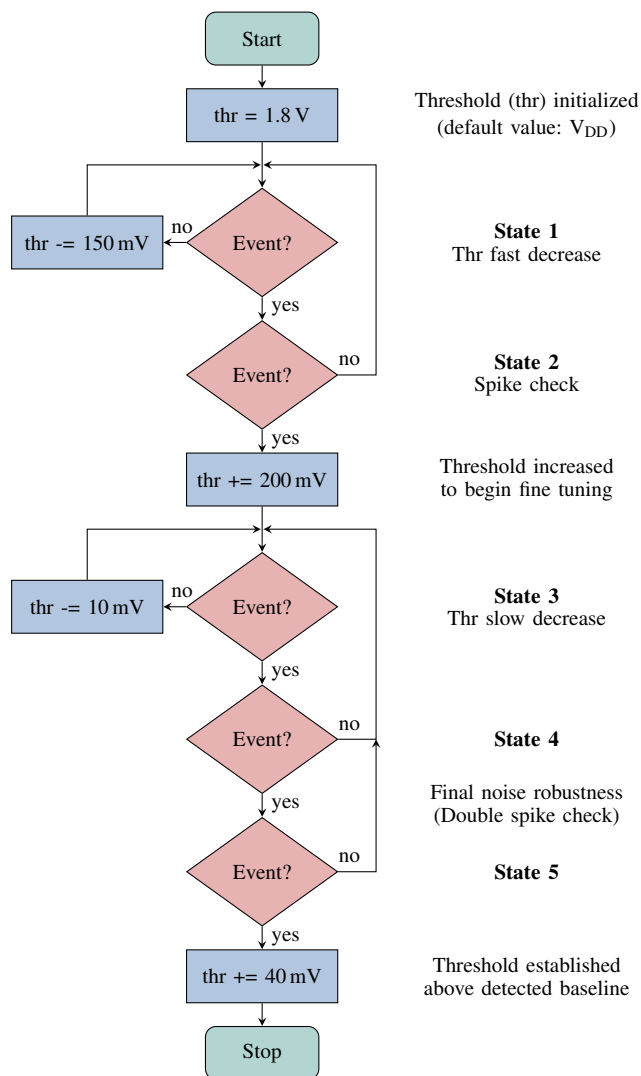

Fig. 14. Firmware routine for threshold auto calibration. The threshold is initialized to a value much higher than the expected signal baseline, and lowered step by step until one or more events arise. The calibration is divided in a first coarse phase, together with a check for spurious spikes, and a second fine tuning, which includes a double spike check, to ensure the final result is correct.

TABLE II
BLE SERVER FOR THE PROPOSED SYSTEM

Characteristic	Handle	Size	Permission[1]
Service Declaration	0x00A0	-	-
Command	0x00A2	1 B-3 B	W
Status	0x00A4	1 B	R/N
Status$_{CCCD}$	0x00A5	2 B	R/W
Gain	0x00A7	1 B	R/W
sEMG	0x00A9	20 B/200 B[2]	N
sEMG$_{CCCD}$	0x00AA	2 B	R/W
Threshold	0x00AC	2 B	R/W
ATC	0x00AE	1 B	N
ATC$_{CCCD}$	0x00AF	2 B	R/W

[1]R: read; W: write; N: notify.   [2]LR/HR

The Bluetooth 4.2 stack perfectly meets these requirements, providing a robust data transfer protocol, with a throughput up to 1 Mbps. According to this, a BLE server has been implemented on the Apollo3 MCU, allowing the user to fully control the device and to get data notifications of the main parameters (i.e., status, ATC and sEMG). The server structure, including handle values, relative size and permissions, is detailed in Table II.

The connection with the device can be established from any remote module, and has to be performed even before initial threshold calibration. Connection parameters can be relaxed, accordingly to low data rate of the ATC technique, selecting a connection interval around the time window chosen for ATC (e.g., if 130 ms has been selected, 60 ms to 80 ms connection interval would fit the application requirements without too much delay). In the case even slower data rate are requested by the user interface, more than one notification could be grouped in a single connection event, widening the connection interval and keeping the transmitter in the idle state for even more time.

The available characteristics (see Table II) can be divided in two main groups: on one side we have Command and Status, one-way channels to control the board behavior and to obtain feedback from it; the remaining ones are all data values, carrying device acquired information and configurations.

In particular, the data characteristics accessibility and behavior are:
- **Gain** contains selected amplification for PGA stage. It accepts values between 1 (default) and 5, and can be read and written: if read, the applied gain is returned; if written, the desired value is loaded in the characteristic and the PGA configuration is updated.
- **sEMG** carries the information about last ADC sampled values. It can only be notified, by writing 1 in its own Client Characteristic Configuration Descriptor (CCCD). Its dimension directly depends on the Maximum Transfer Unit (MTU) selected. Indeed, until BLE 4.1 [48], no more than 20 bytes could be handled. According to this, two configuration have been designed: one at High Resolution

(HR), which can be enabled by requesting an MTU higher than 200, and one at Low Resolution (LR) to assess back-compatibility issues of BLE 4.1 and older versions. In particular, HR mode provides 14-bit values sampled at 1 kHz, resulting in a 2 kB s^{-1} throughput, with BLE connection parameters configured to transmit a 200 B notification every 100 ms. On the other hand, LR configuration provides 8-bit resolution values, sampled at 800 Hz, which is the minimum frequency allowed by Nyquist-Shannon theorem [24] considering our cutoff frequency of 400 Hz (as detailed in Section IV-G). In this case the system would send a 20 B notification every 25 ms, to handle the 0.8 kB s^{-1} application throughput.
- **Threshold** is the 12-bit binary representation of the threshold, as written to the DAC. It accepts values between 0x0000 (0 V) and 0x0FFF (1.8 V). It can be read to check the threshold value (e.g., after the calibration routine) and written to manually set a desired value. In this last case, the DAC output value is automatically updated.
- **ATC** contains last evaluated count of the TC events, as an integer value. No normalization is performed on-board, to avoid complexity increase, and it will be computed by user application only in the case a comparison among different time windows is needed. If a 1 is written in the CCCD, a notification would be sent at the end of each time window. Considering its default 130 ms duration, event-driven processing of sEMG minimizes throughput to 8 B s^{-1}, considerably reducing data amount w.r.t. standard sEMG sampling. Furthermore, this configuration is not constrained by the connection interval and, consequently, by the receiver Bluetooth stack.

The **Status** is enabled by writing a 1 in its CCCD and would send a notification every time an operation terminates or an error occurs. Its idle value is 1, while 0 is the value it holds when the notifications are not enabled.

Last, the **Command** gives the user the permission to execute task on the device. It has a variable dimension (i.e., 1 B to 3 B) attribute, thus allowing different commands to be implemented, without data padding in the array. In particular, these are the actions which can be executed:

- Debug - 1 B - Used to trigger the transmission of the debug status notification, thus checking basic connectivity.
- Gain set - 2 B - Sending this command with a value between 1 ad 5 in the second byte is equivalent to set the gain characteristic at the same value. Returns a Gain_set status in case of success.
- Automatic threshold calibration from V$_{DD}$ - 1 B - The threshold calibration routine is launched, under the Thr_searching status. If a value is found correctly, returns the Thr_found status; if errors occur, a Thr_error status is notified.
- Automatic threshold calibration from *value* - 3 B - Same operation as previous command, but beginning the search from *value*. It should be written in the lower 12 bits of the second and third byte, expressed as resulting by the formula: *value = $2^{12} \cdot Thr/V_{DD}$*.

- Manual threshold set - 3 B - Updates the DAC register with the value contained in the second and third byte, like writing the Threshold characteristic. A Thr_set status should be notified.
- ATC timer set - 2 B - Changes the ATC time window accordingly with the value in the second byte, expressed in milliseconds. Recommended for advanced users only: modifying the window duration without the proper knowledge could bring to poor functionality.

As the reader can notice, while the ATC window can be adjusted by the user, no command is provided to change the raw sEMG sampling period. In fact, the ATC is an arbitrary parameter and could be adapted to different situations, but the sEMG requires a minimum sampling frequency (i.e., at least two times greater than its highest frequency content) to be reconstructed correctly. Thus, being the minimum frequency allowed already selected by default, no user command could be provided to change it.

VI. FROM PROTOTYPE TO SYSTEM PERFORMANCES

This section reports our prototyping and testing phases. The designed PCBs[2], as the one shown in Fig. 16, have been manufactured using standard 4-layers technology, obtaining the total board dimension of 20.5 mm x 33.2 mm x 9.5 mm. The PCB has been organized as follows: the AFE is totally arranged in the bottom layer while MCU, power supply control, charge circuit, and I/O interfaces are placed at the top layer in order to divide as much as possible analog and digital parts, thus exploiting the PCB internal layers for routing the signals tracks and providing the power supply planes. We selected the Artemis Module produced by Sparkfun Electronics [72] for the integration of the Apollo3 Blue MCU into our solution because it integrates into a small package (i.e., 10 mm x 15 mm) all the supporting circuitry (the MCU itself and the RF circuits) needed to access the Ambiq functionalities, also providing an easy programming interface and a standard soldering footprint. Planar connectors

[2]If interested in additional hardware details, the reader can contact one of the authors, which would be pleased to provide further information.
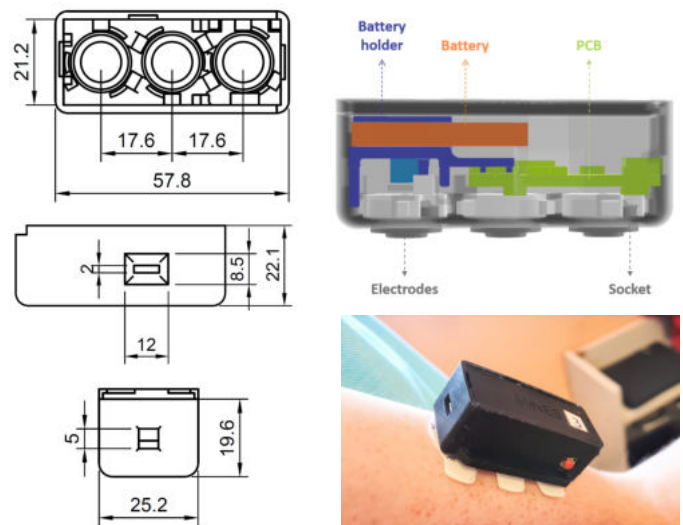

Fig. 17.   Design specification of the 3D-printed case and internal arrangement of PCB, battery and electrodes. Each measure is expressed in mm.

have been used for battery, debug, electrodes, I^{2}C, and reset interfaces in order to save device height. Both JTAG and USB micro-B connectors have been inserted in order to flash the firmware and provide debug operations.

The complete wearable scenario has been finalized by designing the case for the board, also integrating a rechargeable battery and the electrode connectors. Fig. 17 reports the physical dimension and the components organization of our prototype: with an overall dimension of 57.8 mm x 25.2 mm x 22.1 mm, we optimized the packaging by placing the three electrodes (and their connectors) directly below our PCB, which is secured in the right position by the battery holder; a practical hole exhibits the USB micro-B connector allowing to recharge the battery without removing it. Sticky electrodes permits the board to adhere to the body without any additional textile band; on the other hand, dry electrodes required a string to correctly place the case in the proper location above the monitored muscle.

A representative scenario of a typical acquisition setup
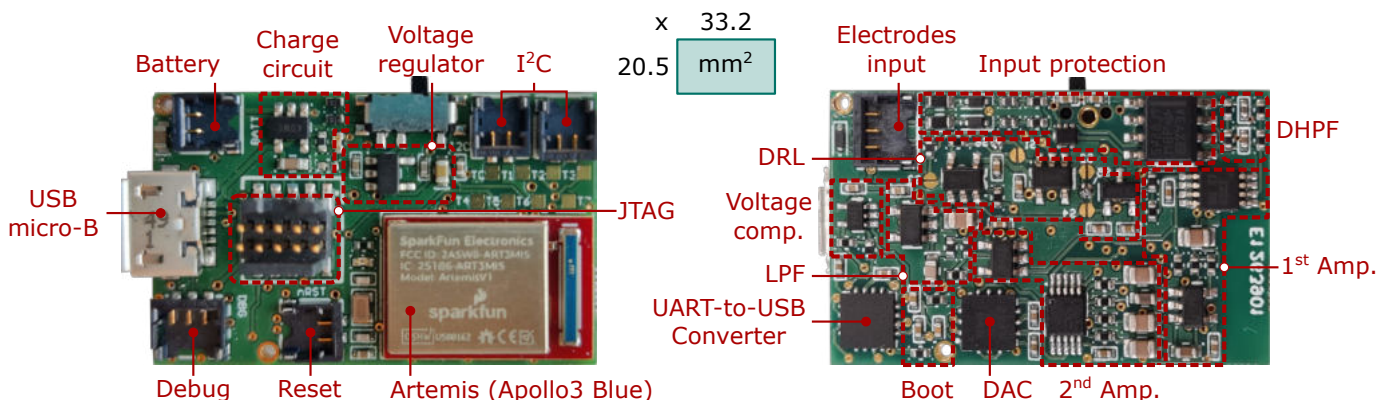

Fig. 16.   Printed Circuit Board (PCB) of the proposed ATC-based wearable module: the electronic components has been organized in order to minimize overall PCB dimension, also taking advantage of the components distribution on both visible layers.
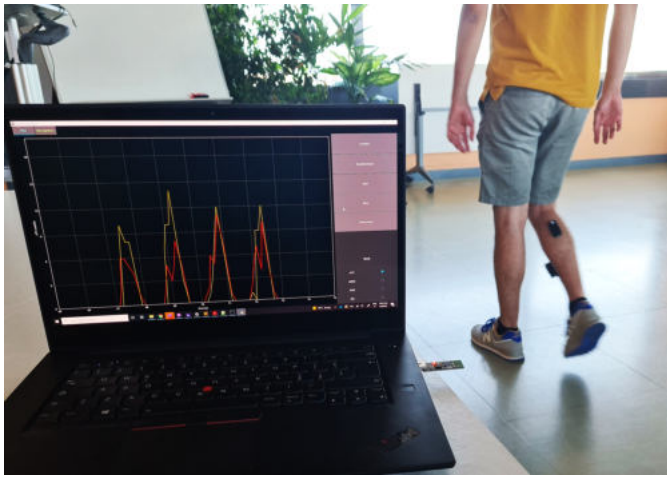
Fig. 18. Example of the system during a gait acquisition: two ATC envelopes are acquired in real-time from the *gastrocnemio medialis* and *soleus* muscle and graphically represented on a user interface.

(here during human walk analysis) is shown in Fig. 18. As it can be seen, a minimal hardware and software configurations are needed to run the system: thanks to the versatility of the BLE protocol, a commercial BLE transceiver (e.g., the CC2540EMK-USB Dongle [73]) could be employed as receiver module, offering a very simple interface between the acquisition board and a custom user-defined interface.

Experimental tests have been conducted in order to analyze the performance of the system for the following points:

- sEMG signal quality;
- ATC extraction;
- Reliability analysis;
- Power consumption.

All the experiments concerning human subjects have been presented to and approved by the Comitato Bioetico di Ateneo of the University of Turin [74].

A. sEMG quality

Considering ATC as the main parameter extracted from sEMG signal, its reliability strictly depends by the integrity of detected muscle information. Therefore, we carried out different tests in order to evaluate if the AFE has been designed correctly.

First, we analyzed how our filters chain responds to input signals, thus verifying the proper band-pass behavior in the 70 Hz to 400 Hz range. By using a National Instruments data acquisition system (i.e., NI USB-6259 [75]), we implemented a LabVIEW script which provides two sine waves with different amplitudes (i.e., 2 mV peak-to-peak difference), at varying frequency (10 Hz to 1000 Hz, 1 Hz step), as channel inputs and, consequently, records filtered and amplified output signal. In Fig. 19 (blue line), we reported the amplitude ratio (dB) between AFE output and the one obtained digital-mathematical processing (theoretical differential flat-band amplification) the *real* (analog) input signals: by imposing −3 dB as acceptability criteria for real/theoretical difference, we figured out that our sEMG conditioning circuit works as expected in the 70 Hz
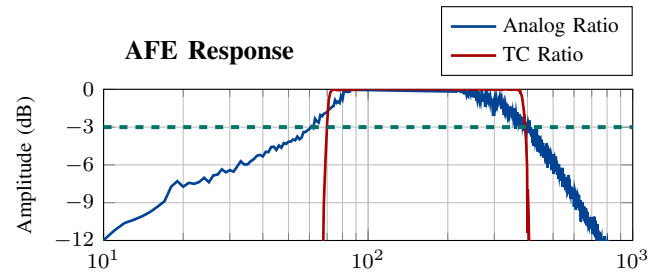

Fig. 19. The graph shows the results of two different characterization analyses for our AFE in the 10 Hz to 1000 Hz frequency range. The first one (blue line) represents the dB ratio between the analog (sEMG) output of the AFE and the theoretical flat-band amplification of its inputs (Section VI-A). A similar analysis (Section VI-B) has been carried out for the analog and simulated TC signal (red line). These measurements confirmed the expected filtering behavior into the 70 Hz to 400 Hz band.

to 400 Hz range, which verifies the DHPF-InAmp feedback combination and anti-aliasing LPF behaviors for low and high spectrum frequencies, respectively.

After checking the response of the AFE, we analyzed if the designed circuitry properly conditions the acquired muscle signal. The sEMG signals have been acquired during the wrist extension movement, placing the sensing electrodes on the *extensor carpi ulnaris* muscle. We standardized motion executions by measuring the Maximum Voluntary Contraction (MVC) with a dynamometer in order to observe how the sampled sEMG adequately represents muscular efforts at 30 % MVC, 70 % MVC, and 100 % MVC values. Both dry [76] and wet [77] electrodes have been compared looking at the Power Spectral Density (PSD) features (see Fig. 20), demonstrating how they could be interchangeable in monitoring different levels of muscle contractions. As expected, the total sEMG energy increases with the raise of MVC, also satisfactory representing
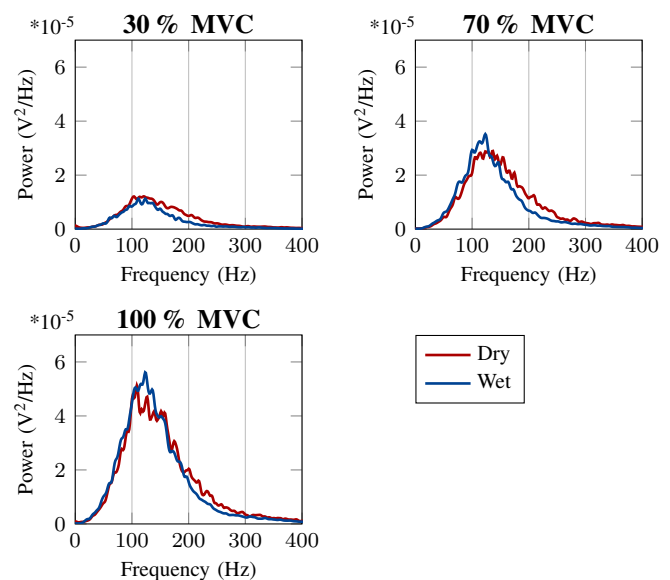

Fig. 20. Comparison among the Power Spectral Density (PSD) of dry and wet electrodes, standardizing the three levels of muscle activation over the Maximum Voluntary Contraction (MVC) (30 % MVC, 70 % MVC, and 100 % MVC)

TABLE III
MONITORED MUSCLES AND RELATED EXECUTABLE MOVEMENTS

Muscle[1]	ID	Movements
Biceps brachii	BB	Elbow Flexion
Triceps brachii	TB	Elbow Extension
Extensor carpi ulnaris	ECU	Wrist Extension
Rectus femoris	RF	Gait, Knee Extension
Vastus lateralis	VL	Gait
Biceps femoris	BF	Gait, Knee Flexion
Tibialis anterior	TA	Gait
Gastrocnemio medialis	GM	Gait
Soleus	SL	Gait

[1] SENIAM guidelines [78] have been followed for electrode placement

the typical frequencies of the sEMG spectrum [23], as it can be noticed in the 50 Hz-150 Hz interval. The calculated PSDs show no influences related to the power-line interference (neither at the 50 Hz central frequency nor at higher harmonics), proving the proper design of the physical circuit (e.g., high accuracy of components selection and PCB layout) and the effectiveness of the AFE filters. However, although dry electrodes present a major noise content above 200 Hz w.r.t wet electrode caused by a more unstable skin-electrode interface, both acquisition setups bring to similar results, demonstrating the system versatility without the need of any adaptations to sensors technology.

Then, we carried out a more detailed analysis acquiring the sEMG signals during the execution of different movements in order to evaluate how our device perform on both upper and lower limb muscles. We executed elbow flexion, knee extension and flexion movements, inducing isometric contractions by employing a set of weights (0 kg, 1 kg, 2 kg, 4 kg). The acquisition protocol, whose biomedical setup is described in Table III, consists of ten repetitions for each movement. We acquired 10 s of sEMG signal after weight stabilization, interrupted by 30 s resting time to avoid the onset of fatigue effects. Signal-to-Noise Ratio (SNR) between the squared powers of the sEMG (P_{sEMG}) and the noise (P_{noise}, here intended as the signal baseline without muscle activity)
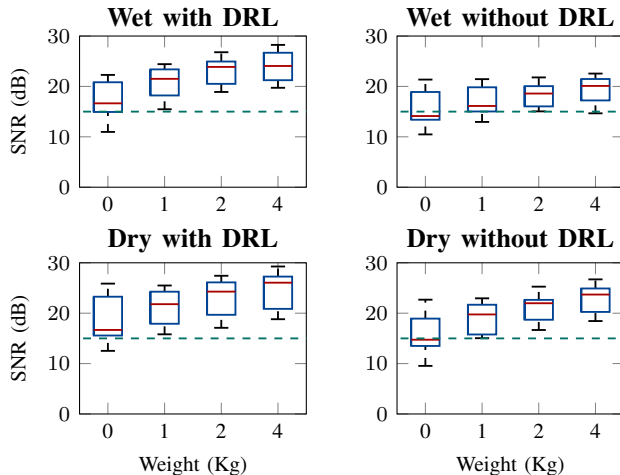

Fig. 21. SNR comparison between wet and dry electrodes, also evaluating the influence of the DRL circuit to drive the reference potential.
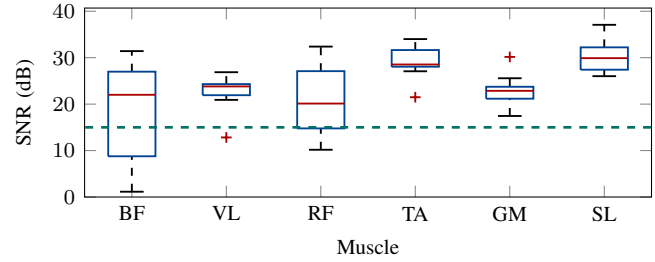

Fig. 22. SNR distribution of the detected sEMG signals in dynamic contractions during human walk. The following multi-muscle acquisition setup has been observed: BF - Biceps Femoris, VL - Vastus Lateralis, RF - Rectus Femoris, TA - Tibialis Anterior, GM - Gastrocnemio Medialis, SL - Soleus.

has been identified as the proper comparison parameter and calculated according to Eq. 6, where both powers have been estimated through the variance (σ^2) of both signal and noise.

$$SNR = 10 \cdot \log_{10}\left(\frac{P_{sEMG}}{P_{noise}}\right)$$
$$= 10 \cdot \log_{10}\left(\frac{\sigma^2_{signal} - \sigma^2_{noise}}{\sigma^2_{noise}}\right) \quad (6)$$

Fig. 21 reports our measurements, where all the exercise repetitions of each monitored muscle are grouped: SNR values increase together with sustained weights resulting in similar outcomes for both wet and dry electrodes, while differences of 5 % to 20 % are clearly visible considering activity of the DRL, hence demonstrating its advantages if configured. An SNR of 15 dB has been identified as a proper threshold to obtain an sEMG signal of a quality more than acceptable [79]: all our measurements here reported largely meet this requirement.

Lastly, we tested our device during the monitoring of dynamic movements, acquiring the sEMG signals from distal and proximal leg muscles (as reported in Table III) during straight human walk. Although this experimental condition could be challenging w.r.t. static muscle analysis, both in terms of signal artifacts and muscular activity, we obtained very satisfactory SNR results (Fig. 22). Boxplots, which group together about 20 steps, demonstrate how our system performs well in real application scenario, fulfilling again the 15 dB acceptability threshold. Boxplots width could vary depending on considered muscle because of its time-varying and multi-function activity in balancing body during straight walk. However, our system detects low activities without compromising the quality of the acquired signals.

To summarize, our simulative and practical tests confirm the proper detection of the sEMG signal (both in static and dynamic conditions), proving the AFE versatility w.r.t. the electrodes typology and the voltage reference configuration depending on the application requirements.

B. ATC Extraction

In order to prove the correctness of hardware TC extraction, we performed two different tests, both involving the NI USB-6259 acquisition system as interface.
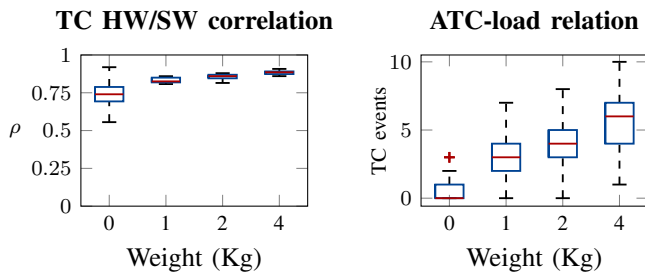
Fig. 23.   TC hardware analysis: (left) cross-correlation with software simulation; (right) validation of direct proportionality with sustained load.

First, we analyzed the TC output signal using a setup similar to the one of the first sEMG response test. In fact, a LabVIEW environment has been configured to generate the two input sine waves, performing the frequency sweep from 10 Hz to 1000 Hz, and to collect the TC signal from the board. Then, TC events are counted over a 130 ms time window and compared with the theoretical ones, simulated without filtering. The obtained ratio (in dB), represented with the red line of Fig. 19, confirms the proper design of the 70 Hz to 400 Hz band-pass filter.

After this simulated analysis, in order to prove the correct behavior of the threshold comparator, we sampled sEMG and TC signals simultaneously, monitoring *biceps brachii* static response at the already standardized set of weights (i.e., 0 kg, 1 kg, 2 kg and 4 kg). sEMG data are then processed in order to compute the threshold crossings, simulating the experimental method and threshold value (also taking into account hysteresis behavior). Fig. 23 shows both the normalized cross-correlation coefficient (ρ) between HW and simulated TC signals and the proportional growth of the HW generated TC events with load increase. The TC events growth validates the direct load proportionality established in [33] and the good correlation w.r.t. the software simulated signal demonstrates the optimal design of the hardware threshold comparator.

C. Reliability Analysis

System reliability has been assessed by comparing the Root Mean Square (RMS) of the sEMG obtained with our device to the one acquired with the Cometa Mini Wave [17] wearable system, which can be identified as a SoA gold standard. In particular, among different indexes present in literature, we have found the Intraclass Correlation Coefficient (ICC) [80] to be the most appropriate to evaluate the robustness of our measures, because it is not influenced by the order of the analyzed samples.

The experimental setup involved a dynamometer to measure stable MVC values, similarly to what we have done in Section VI-A, during wet vs dry electrodes comparison. However, in this test, a set of four movements (elbow flexion, elbow extension, knee flexion, and knee extension) was selected to cover different typologies of muscular activity, acquired following the guidelines of Table III. For each movement, three subjects exerted their MVC in an isotonic position; then, they performed 10 isotonic repetitions at 70 % MVC and 10 at 30 % MVC, with each repetition consisting in 10 s of activation

and 30 s of rest. The same experimental protocol was executed both with our device and with Cometa Mini Wave, in different sessions.

Muscular data were then processed offline to obtain an RMS indicator for each single repetition, in order to proceed with the reliability analysis itself. Considering that the Cometa device and our system have a different acquisition interface (i.e., the Mini Wave has only two electrodes), making a comparison between their respective values would not have been significant, but an intra-rater analysis has been performed to compare how both of them behaved along time. Since the different movements, or contraction levels, are not correlated, we selected the model 1 of the ICC, as suggested in [81], which analyzes the variability of values obtained from different repetitions of the same class (i.e., one combination of person, force and movement). The formula is reported in Eq. 7, where MS_R represents the mean square for the row, intended as the ten repetitions, k is the number of repetitions (i.e., 10), and MS_W is the mean square for residual sources of variance.

$$ICC(1,k) = \frac{MS_R - MS_W}{MS_R + (k-1)MS_W} \qquad (7)$$

While the Cometa Mini Wave scored an ICC of 0.881, our device had a more robust behavior over the different trials reaching a score of 0.934, demonstrating that its reliability is consistent w.r.t. state of the art.

D. Power Consumption

Operational device lifetime is a crucial feature for wearable system which needs to continuously record data providing a stable streaming. Among various HW and SW optimizations (e.g., ultra-low power IC for AFE design, MCU hardware and firmware performance), we tried to minimize as much as possible current absorption during ATC/sEMG data transmission by handling the BLE adjustable parameters (considering relevant transmission power levels), while guaranteeing real-time data accessibility. Keeping in mind protocol constraints, and considering what reported in section V-B, we set variable connection intervals of 12.5 ms to 50 ms and 60 ms to 80 ms

TABLE IV
ENERGY-EFFICIENCY COMPARISON BETWEEN sEMG AND ATC MODES

Mode		TX Power (dBm)				
		-20	**-10**	**-5**	**0**	**4**
CA[1] (mA)	sEMG HR	1.29	1.31	1.30	1.35	1.40
	sEMG LR	2.32	2.32	2.35	2.32	2.42
	ATC[3]	0.46	0.46	0.45	0.46	0.48
OT[2,4] (h)	sEMG HR	85	84	85	82	79
	sEMG LR	47	48	47	48	46
	ATC[3]	237	238	246	240	231
Energy saved (%)	HR	64.1	64.5	65.5	66.0	66.0
	LR	80.0	80.0	81.1	80.2	80.3

[1]CA: Current Absorption   [3]ATC window: 130 ms
[2]OT: Operating Time   [4]110 mAh LiPo battery

in order to successfully achieve sEMG and ATC notifications transmission, respectively.

Table IV reports our measurements, representing mean current absorption (acquired using the DMM7510 digital multimeter [82] sampling at 1 Msample/s) for the three available services (i.e., sEMG at Low Resolution (LR), sEMG at High Resolution (HR), ATC) and the five configurable TX powers (i.e., −20 dBm, −10 dBm, −5 dBm, 0 dBm, 4 dBm). While HR mode is configured for last Bluetooth versions (4.2, 5.0), which, thanks to MTU extension, allow a relaxation of the connection interval (i.e., set to 50 ms), the LR service is designed for back-compatibility with older versions (4.0, 4.1) and requires more strict parameters to keep up with real time application constraints (i.e., connection interval is set to 12.5 ms and sampling frequency is lowered to 800 Hz). Thus, even if the application throughput of LR mode is slightly lower, its shorter connection interval considerably decreases idle periods, increasing overall current absorption.

On the other hand, ATC data reduction (i.e., ~90 %, considering Bluetooth overhead [50]) and further relaxation of connectivity timing (i.e., 60 ms to 80 ms connection interval) allow us to save up to 80 % of required sEMG energy budget, thus leading to about 230 h of constant active transmission (considering the LP401230 Cellevia LiPo battery with 110 mAh capacity [83]), perfectly suitable for long-time monitoring applications.

VII. COMPARISON WITH SoA WORKS

This final section aims to compare the proposed device looking at similar ones, trying to consider both academic and industrial solutions. A comprehensive comparison could be outlined by watching over the application scenario: if on one side commercial devices [17]–[19] are optimized aspiring to provide a satisfying user-experience, but often concealing some technical details from public information, on the other side research activities [20]–[22], [28], [29] provide well-documented analyses, discussing in details the tuning of the leading system parameters, but leaving the door open to further

investigations (no final market-oriented optimization). However, keeping in mind the above disparity, some considerations could be discussed (see Table V) for recent (2018–2021) State-of-Art (SoA) devices.

Since the effectiveness of our solution in sensing the sEMG signals and in extracting the TC (or ATC) information has already been demonstrated, here the comparison points directly to the triplet of size, weight, and operating time features of the device. Their combination perfectly describes the applicability of each system, representing which specifications have been selected in the design phase (e.g., extracted feature, number of sensing channels) and how they have been technically satisfied (e.g., wireless requirements, power consumption).

Therefore, proceeding from the design of the system towards its realization, our prerequisites could be summarized into a stand-alone (single-channel) module for the sEMG/ATC transmission, whose identified and optimized application throughput allowed us to employ ideally the BLE 4.2 wireless technology [49]. Some of the listed SoA works [17], [22], [28], [29] show similar application throughput values (per acquisition channel), demonstrating the validity of our design concept, some of them using the BLE 4.2 [19] protocol as in our solution, and other ones implementing (although not always necessary) more power-consuming solutions such as BlueTooth (BT) 2.0 [20] or WiFi [28], [29].

Combining the sEMG acquisition setting (e.g., sampling rate, ADC resolution), and the feature extraction process (i.e., ATC), with the wireless configuration (e.g., protocol, transmission parameters), we can highlight the differences in terms of power consumption: by completely exploiting the advantages of the ATC approach in reducing the transmission data rate (i.e., 64 bps), and lowering the power supply of the overall on-board circuitry to 1.8 V, we measured an average current absorption under 1 mA during continuous data transmission, making our designed solution quite appealing with respect to other devices [20]–[22].

The above considerations led us to define our prototype properties: with a minimal battery capacity of 110 mAh, we realized the complete case for our device with a volume of

TABLE V
STATE OF THE ART COMPARISON AMONG WEARABLE sEMG ACQUISITION SYSTEMS

Device	Year	Feature	#Ch.	Application Throughput	Wireless Technology	Power Supply	Current Absorption	Battery	Size	Weight	Operating Time
[17]	2021	sEMG	1	32 kbps	n.a.	n.a.	n.a.	n.a.	5.0 cm^3	7 g	12 h
[18]	2021	sEMG	1	n.a.	WiFi	n.a.	n.a.	n.a.	14.1 cm^3	17 g	8 h
[19]	2021	sEMG	1	n.a.	Proprietary RF BLE 4.2	n.a.	n.a.	n.a.	13.0 cm^3	14 g	8 h
[20]	2021	sEMG	4	n.a.	BT 2.0	n.a.	46 mA	700 mAh	78.2 cm^3	140 g	15 h
[21]	2019	sEMG	32	1.04 Mbps	WiFi	3.3 V	119 mA	600 mAh	15.3 cm^3	16.7 g	5 h
[22]	2021	sEMG	8	384 kbps	BLE 5.0	5 V	105 mA	600 mAh	22.0 cm^3	41.7 g	5 h
[28]	2018	sEMG	8	192 kbps	WiFi	± 3 V	n.a.	700 mAh	n.a.	n.a.	n.a.
[29]	2020	sEMG	1	32 kbps	WiFi	n.a.	n.a.	300 mAh	n.a.	n.a.	n.a.
This work	2021	sEMG ATC	1	16 kbps 64 bps	BLE 4.2	1.8 V	1.40 mA 0.48 mA	110 mAh	32.2 cm^3	27.4 g	80 h 231 h

$32.2\,\mathrm{cm}^3$ (including bio-potential electrodes, mounted at the bottom side, as represented in Fig. 17) and a total weight of $27.4\,\mathrm{g}$. Both fall within the average of those found in the various works reported in Table V, identifying our solution compatible with current SoA wearable sEMG devices.

Lastly, since we developed the proposed solution aiming to overcome the functional timing limitations, we could take a final look at the operating time: all selected SoA works show a total duration of at least $15\,\mathrm{h}$, even practically lowered to $5\,\mathrm{h}$ or $8\,\mathrm{h}$, which adequately fits the time-requirements of clinical procedures but does not allow to achieve a constant monitoring for daily-life activities (e.g., up to $24\,\mathrm{h}$ to $48\,\mathrm{h}$). In contrast, the different optimizations disclosed in this tutorial permit us to reach a steady sEMG transmission of $80\,\mathrm{h}$, or, additionally enabling the benefits of the ATC approach, to cover an event-driven acquisition of a week.

In conclusion, looking at Table V in its entirety, we can observe how the proposed device fits harmoniously into this application scenario, adequately withstanding current academic or industrial solutions [17]–[19], [21] while providing satisfactory improvements in terms of total operating time.

VIII. Conclusion

This tutorial guided the reader towards the design of a wearable bio-inspired system for sEMG acquisition. After a preliminary introduction about our event-driven hardware feature extraction (ATC), which extends operating time relaxing power consumption, the general framework has been defined, selecting the Apollo3 Blue MCU as central core of the system. Then, an accurate selection of each single component of the acquisition channel is performed, analyzing the difference outcome of multiple approaches, followed by the definition of the firmware routines needed to handle sampling and communication concurrently.

The resulting device was tested under various scenarios, obtaining several performance estimation. In particular, regarding the sEMG signal, an SNR of more than $15\,\mathrm{dB}$ has been measured, with an application throughput of $2\,\mathrm{kB}\,\mathrm{s}^{-1}$ and a battery life of more than $80\,\mathrm{h}$. The ATC hardware extraction has been compared with a simulated threshold crossing feature, confirming the reliability of the hardware design and the correlation with the exerted force. In the lowest energy consuming configuration, the device sends only the $8\,\mathrm{B}\,\mathrm{s}^{-1}$ required by the ATC technique, obtaining a continuous operating time up to $230\,\mathrm{h}$.
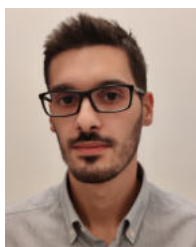
The promising results of the proposed design confirm our effort in the bio-inspired direction, thus strengthening our vision towards future implementations, which will completely evolve the current sEMG-ATC sensor module into a multi-channel muscular monitoring system suitable for several applications.

References

[1] J. Cram, "The history of surface electromyography," *Applied psychophysiology and biofeedback*, vol. 28, pp. 81–91, 07 2003.

[2] R. Merletti, A. Botter, and U. Barone, *Detection and Conditioning of Surface EMG Signals*. John Wiley & Sons, Ltd, 2016, ch. 3, pp. 1–37. [Online]. Available: https://onlinelibrary.wiley.com/doi/abs/10.1002/9781119082934.ch03

[3] C. Steele, *Applications of EMG in Clinical and Sports Medicine*. IntechOpen. [Online]. Available: https://www.intechopen.com/books/applications-of-emg-in-clinical-and-sports-medicine

[4] I. Campanini, C. Disselhorst-Klug, W. Z. Rymer, and R. Merletti, "Surface EMG in clinical assessment and neurorehabilitation: Barriers limiting its use," *Frontiers in Neurology*, vol. 11, p. 934, 2020. [Online]. Available: https://www.frontiersin.org/article/10.3389/fneur.2020.00934

[5] R. Pilkar, K. Momeni, A. Ramanujam, M. Ravi, E. Garbarini, and G. F. Forrest, "Use of surface EMG in clinical rehabilitation of individuals with SCI: Barriers and future considerations," *Frontiers in Neurology*, vol. 11, p. 1680, 2020. [Online]. Available: https://www.frontiersin.org/article/10.3389/fneur.2020.578559

[6] P. Leelaarporn, P. Wachiraphan, T. Kaewlee, T. Udsa, R. Chaisaen, T. Choksatchawathi, R. Laosirirat, P. Lakhan, P. Natnithikarat, K. Thanontip, W. Chen, S. C. Mukhopadhyay, and T. Wilaiprasitporn, "Sensor-driven achieving of smart living: A review," *IEEE Sensors Journal*, vol. 21, no. 9, pp. 10 369–10 391, 2021.

[7] G. Biagetti, P. Crippa, L. Falaschetti, and S. Orcioni, "Human activity monitoring system based on wearable sEMG and accelerometer wireless sensor nodes," *BioMedical Engineering OnLine*, vol. 17, 11 2018.

[8] C. Prahm, I. Vujaklija, F. Kayali, P. Purgathofer, and O. C. Aszmann, "Game-based rehabilitation for myoelectric prosthesis control," *JMIR Serious Games*, vol. 5, no. 1, p. e3, Feb 2017. [Online]. Available: https://games.jmir.org/2017/1/e3/

[9] A. Soares, E. Lamounier Júnior, A. Andrade, and A. Cardoso, *Virtual and Augmented Reality: A New Approach to Aid Users of Myoelectric Prostheses*, 10 2012.

[10] M. Simão, N. Mendes, O. Gibaru, and P. Neto, "A review on electromyography decoding and pattern recognition for human-machine interaction," *IEEE Access*, vol. 7, pp. 39 564–39 582, 2019.

[11] L. Bi, A. G. Feleke, and C. Guan, "A review on EMG-based motor intention prediction of continuous human upper limb motion for human-robot collaboration," *Biomedical Signal Processing and Control*, vol. 51, pp. 113–127, 2019. [Online]. Available: https://www.sciencedirect.com/science/article/pii/S1746809419300473

[12] G. Meltzner, J. Heaton, Y. Deng, G. Luca, S. Roy, and J. Kline, "Development of sEMG sensors and algorithms for silent speech recognition," *Journal of Neural Engineering*, vol. 15, 06 2018.

[13] A. Calado, F. Soares, and D. Matos, "A review on commercially available anthropomorphic myoelectric prosthetic hands, pattern-recognition-based microcontrollers and sEMG sensors used for prosthetic control," in *2019 IEEE International Conference on Autonomous Robot Systems and Competitions (ICARSC)*, 2019, pp. 1–6.

[14] K. Li, J. Zhang, L. Wang, M. Zhang, J. Li, and S. Bao, "A review of the key technologies for sEMG-based human-robot interaction systems," *Biomedical Signal Processing and Control*, vol. 62, p. 102074, 2020. [Online]. Available: https://www.sciencedirect.com/science/article/pii/S1746809420302305

[15] Digital Science & Research Solutions, Inc. "surface electromyography" in Publications - Dimension. Accessed: August 6, 2021. [Online]. Available: https://app.dimensions.ai/discover/publication?search_mode=content&search_text=%22surface%20electromyography%22&search_type=kws&search_field=full_search

[16] National Library of Medicine. "surface electromyography" - Search Results - PubMed. Accessed: August 6, 2021. [Online]. Available: https://pubmed.ncbi.nlm.nih.gov/?term=surface+electromyography&timeline=expanded

[17] Cometa srl. Cometa systems. Accessed: August 6, 2021. [Online]. Available: https://www.cometasystems.com/

[18] Biometrics Ltd. Surface EMG sensor. Accessed: August 6, 2021. [Online]. Available: https://www.biometricsltd.com/surface-emg-sensor.htm

[19] Delsys Incorporated. Delsys family of products. Accessed: August 6, 2021. [Online]. Available: https://delsys.com/products/

[20] PLUX Wireless Biosignals S.A. BITalino (r)evolution MuscleBIT BT. Accessed: August 6, 2021. [Online]. Available: https://bitalino.com/products/musclebit-bt

[21] G. L. Cerone, A. Botter, and M. Gazzoni, "A modular, smart, and wearable system for high density sEMG detection," *IEEE Transactions on Biomedical Engineering*, vol. 66, no. 12, pp. 3371–3380, 2019.

[22] L. Zhu, G. Mao, H. Su, Z. Zhou, W. Li, X. Lü, and Z. Wang, "A wearable, high-resolution, and wireless system for multichannel surface electromyography detection," *IEEE Sensors Journal*, vol. 21, no. 8, pp. 9937–9948, 2021.

[23] C. J. De Luca, *Surface Electromyography: Detection and Recording*. DelSys Incorporated, 2002.

[24] G. De Luca, *Fundamental Concepts in EMG Signal Acquisition*. DelSys Incorporated, 2001.

[25] B. Gao, C. Wei, H. Ma, S. Yang, X. Ma, and S. Zhang, "Real-time evaluation of the signal processing of sEMG used in limb exoskeleton rehabilitation system," *Applied Bionics and Biomechanics*, vol. 2018, pp. 1–6, 10 2018.

[26] K.-M. Chang, S.-H. Liu, and X.-H. Wu, "A wireless sEMG recording system and its application to muscle fatigue detection," *Sensors*, vol. 12, no. 1, pp. 489–499, 2012. [Online]. Available: https://www.mdpi.com/1424-8220/12/1/489

[27] D. Brunelli, E. Farella, D. Giovanelli, B. Milosevic, and I. Minakov, "Design considerations for wireless acquisition of multichannel sEMG signals in prosthetic hand control," *IEEE Sensors Journal*, vol. 16, no. 23, pp. 8338–8347, 2016.

[28] M. Ergeneci, K. Gokcesu, E. Ertan, and P. Kosmas, "An embedded, eight channel, noise canceling, wireless, wearable sEMG data acquisition system with adaptive muscle contraction detection," *IEEE Transactions on Biomedical Circuits and Systems*, vol. 12, no. 1, pp. 68–79, 2018.

[29] Y.-H. Yang, S.-J. Ruan, P.-C. Chen, Y.-T. Liu, and Y.-H. Hsueh, "A low-cost wireless multichannel surface EMG acquisition system," *IEEE Consumer Electronics Magazine*, vol. 9, no. 5, pp. 14–19, 2020.

[30] A. Prakash, B. Kumari, and S. Sharma, "A low-cost, wearable sEMG sensor for upper limb prosthetic application," *Journal of Medical Engineering & Technology*, vol. 43, no. 4, pp. 235–247, 2019, pMID: 31414614. [Online]. Available: https://doi.org/10.1080/03091902.2019.1653391

[31] SparkFun Electronics®. MyoWare muscle sensor kit. Accessed: August 6, 2021. [Online]. Available: https://learn.sparkfun.com/tutorials/myoware-muscle-sensor-kit

[32] P. Motto Ros, A. Sanginario, M. Crepaldi, and D. Demarchi, "Quality-energy trade-off and bio-inspired electronic systems," in *2018 IEEE International Conference on the Science of Electrical Engineering in Israel (ICSEE)*, 2018, pp. 1–5.

[33] S. Sapienza, M. Crepaldi, P. Motto Ros, A. Bonanno, and D. Demarchi, "On integration and validation of a very low complexity ATC UWB system for muscle force transmission," *IEEE Transactions on Biomedical Circuits and Systems*, vol. 10, no. 2, pp. 497–506, 2016.

[34] F. Rossi, P. Motto Ros, S. Sapienza, P. Bonato, E. Bizzi, and D. Demarchi, *Wireless Low Energy System Architecture for Event-Driven Surface Electromyography*. Springer, 05 2019, pp. 179–185.

[35] S. Sapienza, P. Motto Ros, D. A. Fernandez Guzman, F. Rossi, R. Terracciano, E. Cordedda, and D. Demarchi, "On-line event-driven hand gesture recognition based on surface electromyographic signals," in *2018 IEEE International Symposium on Circuits and Systems (ISCAS)*, 2018, pp. 1–5.

[36] A. Mongardi, F. Rossi, P. Motto Ros, A. Sanginario, M. Ruo Roch, M. Martina, and D. Demarchi, "Live demonstration: Low power embedded system for event-driven hand gesture recognition," in *2019 IEEE Biomedical Circuits and Systems Conference (BioCAS)*, 2019, pp. 1–1.

[37] A. Mongardi, P. Motto Ros, F. Rossi, M. Ruo Roch, M. Martina, and D. Demarchi, "A low-power embedded system for real-time sEMG based event-driven gesture recognition," in *2019 26th IEEE International Conference on Electronics, Circuits and Systems (ICECS)*, 2019, pp. 65–68.

[38] F. Rossi, P. Motto Ros, and D. Demarchi, "Live demonstration: Low power system for event-driven control of functional electrical stimulation," in *2018 IEEE International Symposium on Circuits and Systems (ISCAS)*, 2018, pp. 1–1.

[39] F. Rossi, R. M. Rosales, P. Motto Ros, and D. Demarchi, "Real-time embedded system for event-driven sEMG acquisition and functional electrical stimulation control," in *Applications in Electronics Pervading Industry, Environment and Society*. Springer, Cham, 2019.

[40] F. Rossi, P. Motto Ros, S. Cecchini, A. Crema, S. Micera, and D. Demarchi, "An event-driven closed-loop system for real-time FES control," in *2019 26th IEEE International Conference on Electronics, Circuits and Systems (ICECS)*, 2019, pp. 867–870.

[41] F. Rossi, P. Motto Ros, R. M. Rosales, and D. Demarchi, "Embedded bio-mimetic system for functional electrical stimulation controlled by event-driven sEMG," *Sensors*, vol. 20, no. 5, 2020. [Online]. Available: https://www.mdpi.com/1424-8220/20/5/1535

[42] R. Barioul, S. Fakhfakh, H. Derbel, and O. Kanoun, "Evaluation of EMG signal time domain features for hand gesture distinction," in *2019 16th International Multi-Conference on Systems, Signals Devices (SSD)*, 2019, pp. 489–493.

[43] D. C. Toledo-Pérez, J. Rodríguez-Reséndiz, and R. A. Gómez-Loenzo, "A study of computing zero crossing methods and an improved proposal for EMG signals," *IEEE Access*, vol. 8, pp. 8783–8790, 2020.

[44] M. Crepaldi, M. Paleari, A. Bonanno, A. Sanginario, P. Ariano, D. H. Tran, and D. Demarchi, "A quasi-digital radio system for muscle force transmission based on event-driven IR-UWB," in *2012 IEEE Biomedical Circuits and Systems Conference (BioCAS)*, 2012, pp. 116–119.

[45] P. Motto Ros, M. Paleari, N. Celadon, A. Sanginario, A. Bonanno, M. Crepaldi, P. Ariano, and D. Demarchi, "A wireless address-event representation system for ATC-based multi-channel force wireless transmission," *5th IEEE International Workshop on Advances in Sensors and Interfaces IWASI*, pp. 51–56, 2013.

[46] D. A. Fernandez Guzman, S. Sapienza, B. Sereni, and P. Motto Ros, "Very low power event-based surface EMG acquisition system with off-the-shelf components," in *2017 IEEE Biomedical Circuits and Systems Conference (BioCAS)*, 2017, pp. 1–4.

[47] A. Shahshahani, M. Shahshahani, P. Motto Ros, A. Bonanno, M. Crepaldi, M. Martina, D. Demarchi, and G. Masera, "An all-digital spike-based ultra-low-power IR-UWB dynamic average threshold crossing scheme for muscle force wireless transmission," in *2015 Design, Automation Test in Europe Conference Exhibition (DATE)*, 2015, pp. 1479–1484.

[48] Bluetooth SIG Inc. Bluetooth specification version 4.1. Accessed: August 6, 2021. [Online]. Available: https://www.bluetooth.com/specifications/specs/core-specification-4-1/

[49] Bluetooth SIG Inc. Bluetooth specification version 4.2. Accessed: August 6, 2021. [Online]. Available: https://www.bluetooth.com/specifications/specs/core-specification-4-2/

[50] J. Tosi, F. Taffoni, M. Santacatterina, R. Sannino, and D. Formica, "Performance evaluation of bluetooth low energy: A systematic review," *Sensors*, vol. 17, no. 12, 2017. [Online]. Available: https://www.mdpi.com/1424-8220/17/12/2898

[51] Microchip Technology, Inc. Bluetooth® low energy packet types. Accessed: August 6, 2021. [Online]. Available: http://microchipdeveloper.com/wireless:ble-link-layer-packet-types

[52] P. Motto Ros, B. Miccoli, A. Sanginario, and D. Demarchi, "Low-power architecture for integrated CMOS bio-sensing," in *2017 IEEE Biomedical Circuits and Systems Conference (BioCAS)*, 2017, pp. 1–4.

[53] Ambiq Micro. Apollo3 Blue. Accessed: August 6, 2021. [Online]. Available: https://ambiq.com/apollo3-blue/

[54] Nordic Semiconductor. nRF52840. Accessed: August 6, 2021. [Online]. Available: https://www.nordicsemi.com/Products/Low-power-short-range-wireless/nRF52840

[55] Texas Instruments. CC2642R. Accessed: August 6, 2021. [Online]. Available: https://www.ti.com/product/CC2642R

[56] ST Microelectronics. STM32WB55VG. Accessed: August 6, 2021. [Online]. Available: https://www.st.com/en/microcontrollers-microprocessors/stm32wb55vg.html

[57] NXP. QN908x: Ultra-Low-Power Bluetooth Low Energy System on Chip Solution. Accessed: August 6, 2021. [Online]. Available: https://www.nxp.com/products/wireless/bluetooth-low-energy/qn908x-ultra-low-power-bluetooth-low-energy-system-on-chip-solution:QN9080

[58] R. Merletti and S. Muceli, "Tutorial. surface EMG detection in space and time: Best practices," *Journal of Electromyography and Kinesiology*, vol. 49, p. 102363, 2019. [Online]. Available: https://www.sciencedirect.com/science/article/pii/S1050641119302536

[59] C. J. De Luca, L. Donald Gilmore, M. Kuznetsov, and S. H. Roy, "Filtering the surface EMG signal: Movement artifact and baseline noise contamination," *Journal of Biomechanics*, vol. 43, no. 8, pp. 1573–1579, 2010. [Online]. Available: https://www.sciencedirect.com/science/article/pii/S0021929010000631

[60] R. Merletti and G. Cerone, "Tutorial. surface EMG detection, conditioning and pre-processing: Best practices," *Journal of Electromyography and Kinesiology*, vol. 54, p. 102440, 2020. [Online]. Available: https://www.sciencedirect.com/science/article/pii/S1050641120300821

[61] E. M. Spinelli, R. Pallas-Areny, and M. A. Mayosky, "AC-coupled front-end for biopotential measurements," *IEEE Transactions on Biomedical Engineering*, vol. 50, no. 3, pp. 391–395, 2003.

[62] Texas Instruments, *INA333 Micro-Power (50 μA), Zerø-Drift, Rail-to-Rail Out Instrumentation Amplifier*. [Online]. Available: https://www.ti.com/product/INA333

[63] E. Spinelli and F. Guerrero, *Chapter 12-THE BIOLOGICAL AMPLIFIER*. World Scientific, 07 2019.

[64] S. Franco, *Design with operational amplifiers and analog integrated circuits*, McGraw-Hill's, Ed.

[65] B. B. Winter and J. G. Webster, "Driven-right-leg circuit design," *IEEE Transactions on Biomedical Engineering*, vol. BME-30, no. 1, pp. 62–66, 1983.

[66] E. Spinelli, N. Martinez, and M. Mayosky, "A transconductance driven-right-leg circuit," *IEEE Transactions on Biomedical Engineering*, vol. 46, no. 12, pp. 1466–1470, 1999.

[67] M. Haberman and E. Spinelli, "A digital driven right leg circuit," in *2010 Annual International Conference of the IEEE Engineering in Medicine and Biology*, 2010, pp. 6559–6562.

[68] Y. G. Lim, G. S. Chung, and K. S. Park, "Capacitive driven-right-leg grounding in indirect-contact ecg measurement," in *2010 Annual International Conference of the IEEE Engineering in Medicine and Biology*, 2010, pp. 1250–1253.

[69] R. Mahajan and B. I. Morshed, "Performance analysis of a DRL-less AFE for battery-powered wearable EEG," *Measurement*, vol. 90, pp. 583–591, 2016. [Online]. Available: https://www.sciencedirect.com/science/article/pii/S0263224116301075

[70] X.-B. Chen, Y.-X. Zhou, H.-P. Wang, X.-Y. Lü, and Z.-G. Wang, "Design of sEMG-detecting circuit for EMG-bridge," in *2017 39th Annual International Conference of the IEEE Engineering in Medicine and Biology Society (EMBC)*, 2017, pp. 382–385.

[71] Amazon Web Services, Inc. FreeRTOS: Real-time operating system for microcontrollers. Accessed: August 6, 2021. [Online]. Available: https://www.freertos.org/

[72] SparkFun Electronics®. ARTEMIS FEATURES. Accessed: August 6, 2021. [Online]. Available: https://www.sparkfun.com/artemis

[73] Texas Instruments. CC2540EMK-USB Bluetooth Low Energy and proprietary wireless MCU. Accessed: August 6, 2021. [Online]. Available: https://www.ti.com/tool/CC2540EMK-USB

[74] Università degli Studi di Torino. Comitato di bioetica dell'ateneo. Accessed: August 6, 2021. [Online]. Available: https://www.unito.it/ricerca/strutture-e-organi-la-ricerca/comitato-di-bioetica-dellateneo

[75] National Instruments Corp. USB-6259 - multifunction I/O device. Accessed: August 6, 2021. [Online]. Available: https://www.ni.com/it-it/support/model.usb-6259.html

[76] BITalino. Non-gelled Reusable Ag/AgCl. Accessed: August 6, 2021. [Online]. Available: https://plux.info/electrodes/60-non-gelled-reusable-agagcl-electrodes-870122114.html

[77] Cardinal Health. Kendall H124SG Electrodes. Accessed: August 6, 2021. [Online]. Available: https://www.cardinalhealth.co.uk/en_gb/medical-products/patient-care/electrocardiography/adult-monitoring-electrodes/general-monitoring-ecg-electrodes/long-term-electrodes/kendall-electrodes-h124sg.html

[78] H. Hermens, B. Freriks, R. Merletti, G. Rau, C. Disselhorst-Klug, D. Stegeman, and G. Hägg. SENIAM project. Accessed: August 6, 2021. [Online]. Available: http://www.seniam.org/

[79] Delsys Incorporated. How to improve EMG signal quality: The Signal to Noise Ratio (SNR). Accessed: August 6, 2021. [Online]. Available: https://delsys.com/emgworks/signal-quality-monitor/improve/

[80] D. Liljequist, B. Elfving, and K. Skavberg Roaldsen, "Intraclass correlation – a discussion and demonstration of basic features," *PLOS ONE*, vol. 14, no. 7, pp. 1–35, 07 2019. [Online]. Available: https://doi.org/10.1371/journal.pone.0219854

[81] T. K. Koo and M. Y. Li, "A guideline of selecting and reporting intraclass correlation coefficients for reliability research," *Journal of chiropractic medicine*, vol. 15, no. 2, pp. 155–163, 2016. [Online]. Available: https://www.ncbi.nlm.nih.gov/pmc/articles/PMC4913118/pdf/main.pdf

[82] Tektronix. DMM7510. Accessed: August 6, 2021. [Online]. Available: https://www.tek.com/tektronix-and-keithley-digital-multimeter/dmm7510

[83] Cellevia Batteries. Polymer lithium-ion battery. Accessed: August 6, 2021. [Online]. Available: https://www.tme.eu/Document/006a3b26c26b8c02553cf3dfa2199a63/lp401230_110mah.pdf

Andrea Mongardi (M'18) received both his Bachelor in electronic engineering and the Master in electronic engineering, embedded systems specialization, from Politecnico di Torino, Turin, Italy, in 2017 and 2019, respectively.

Since November 2020 he is a PhD candidate at Politecnico di Torino, Department of Electronics and Telecommunications, focusing on the design of low power embedded systems for sEMG acquisition, and member of the Micro and Nano Electronic Systems (MiNES) Laboratory.

Paolo Motto Ros (M'16) received the Engineering and Ph.D. degrees in electronic engineering from the Politecnico di Torino (IT), in 2005 and 2009, respectively.

He is Senior Post-Doctoral Researcher and Adjunct Professor at Politecnico di Torino (IT), Dipartimento di Elettronica e Telecomunicazioni, with the MiNES (Micro&Nano Electronic Systems) group. From 2009 to 2012, he was with Politecnico di Torino as Postdoc Researcher (jointly with, 2009–2013, Istituto Nazionale Fisica Nucleare, INFN, IT). From 2012 to 2019, he was with Istituto Italiano di Tecnologia as Senior (since 2014) Postdoc Researcher; current research interests include: event-driven digital integrated circuits, architectures, and systems; low-power smart sensor networks; bio-inspired electronics; biomedical and humanoid robotic applications. He counts more than 60 publications.

Dr. Motto Ros is member of the IEEE CAS Society. He was member of the organizing staff of the IEEE BioCAS 2017 conference, and member of the organizing committee of the IEEE ICECS 2019 conference and the FoodCAS Satellite Event at the IEEE ISCAS 2021 conference. He is guest editor of MDPI Sensors and topic editor of Frontiers in Neurorobotics.

Fabio Rossi (GSM'20) received both his Bachelor and Master degrees in Biomedical Engineering from Politecnico di Torino, Turin, Italy, in 2015 and 2017, respectively.

He started his Ph.D. studies in electronic engineering since November 2018, at Politecnico di Torino, Department of Electronic and Telecommunication. Research interests are focused on design of low-power systems for medical bio-electronic applications. Since 2016 he is member of Micro and Nano Electronic System (MiNES) research group.

Massimo Ruo Roch (M'20) received the M.S. and Ph.D. degrees in electrical engineering from the Politecnico di Torino, Italy, in 1989 and 1993, respectively.

He is currently an Assistant Professor from the VLSI-Lab Group, Politecnico di Torino. His research interests include VLSI design and implementation of architectures for digital signal processing, communications, embedded systems design, smart systems with distributed intelligence, logic in memory architectures, and cad tools for nanotechnology based architectures. He is co-author of more then 60 papers.

Maurizio Martina (M'04, SM'15) received the M.S. and Ph.D. degrees in electrical engineering from the Politecnico di Torino, Italy, in 2000 and 2004, respectively.

He is currently an Associate Professor from the VLSI-Lab Group, Politecnico di Torino. His research interests include VLSI design and implementation of architectures for digital signal processing, video coding, communications, artificial intelligence, machine learning, and event-based processing. He edited one book and published three book chapters on VLSI architectures and digital circuits for video coding, wireless communications, and error correcting codes. He has more than 100 scientific publications and is coauthor of two patents.

Prof. Martina is currently an Associate Editor of the IEEE Transactions on Circuits and Systems—I: Regular Papers. He had been part of the Organizing and Technical Committee of several international conferences, including BioCAS 2017, ICECS 2019, and AICAS 2020. He is also the Counselor of the IEEE Student Branch at the Politecnico di Torino and a Professional Member of IEEE HKN.

Danilo Demarchi (M'10-SM'13) received Engineering Degree and Ph.D. in electronics engineering from Politecnico di Torino, Italy, in 1991 and 1995, respectively.

Full position as Associate Professor at Politecnico di Torino, Department of Electronics and Telecommunications, Turin, Italy. Visiting Professor at Tel Aviv University (2018-2021) and at EPFL Lausanne (2019). Visiting Scientist at MIT and Harvard Medical School (2018). Author and co-author of 5 patents and more than 250 international scientific publications.

Prof. Demarchi is the leader of the MiNES (Micro&Nano Electronic Systems) Laboratory at Politecnico di Torino, Member of the BioCAS Technical Committee, Associate Editor of IEEE Sensors Journal and of the Springer Journal BioNanoScience, Member of IEEE Sensors Council, General Chair of IEEE BioCAS 2017 and founder of the IEEE FoodCAS Workshop (Circuits and Systems for the Food Chain).